MRI-Related Heating of Implants and Devices: A Review

Lukas Winter, PhD,[1] Frank Seifert, PhD,[1] Luca Zilberti, PhD,[2] Manuel Murbach, PhD,[3,4] and Bernd Ittermann, PhD[1]*

During an MRI scan, the radiofrequency field from the scanner's transmit coil, but also the switched gradient fields, induce currents in any conductive object in the bore. This makes any metallic medical implant an additional risk for an MRI patient, because those currents can heat up the surrounding tissues to dangerous levels. This is one of the reasons why implants are, until today, considered a contraindication for MRI; for example, by scanner manufacturers. Due to the increasing prevalence of medical implants in our aging societies, such general exclusion is no longer acceptable. Also, it should be no longer needed, because of a much-improved safety-assessment methodology, in particular in the field of numerical simulations. The present article reviews existing literature on implant-related heating effects in MRI. Concepts for risk assessment and quantification are presented and also some first attempts towards an active safety management and risk mitigation.

Level of Evidence: 5
Technical Efficacy: Stage 5

J. MAGN. RESON. IMAGING 2020.

MAGNETIC RESONANCE IMAGING (MRI) scanners utilize static and time-varying electromagnetic (EM) fields to image human subjects. Even when interacting with "native," that is, purely biological, tissues these EM fields can pose a hazard for the patient; for example, by excessive tissue heating due to the transmitted radiofrequency (RF) field. While still an active field of research, a high level of understanding has been achieved for these phenomena and mature safety provisions have emerged from this knowledge. The situation becomes more complicated when a patient carries a medical implant, in particular if that device contains metallic, that is, electrically conductive, parts.

By the physical nature of their interaction, patient hazards in MRI due to the presence of metallic implants can be grouped into four categories: 1) forces and torques on ferromagnetic objects due to the static magnetic field B_0; 2) forces, sometimes referred to as Lenz forces, and related torques exerted by the static magnetic field on moving metallic objects (also if nonferromagnetic); 3) malfunction of an active device; for example, a cardiac pacemaker, because of the strong EM fields in MRI, resulting in missing support of vital functions or even active damage by erratic behavior; 4) local heating and resulting tissue damage due to currents in the implant induced by the time-varying RF and gradient fields.[1,2]

Today's scanners are built to image biological tissues but not to deal with metallic objects: they have no means to automatically detect and adjust to them even though the implemented safety measures are no longer adequate in the presence of metals.[3] Ultimately, appropriate safety concepts for scanning implant carriers must be implemented at the *system level*; scanners must detect an implant and respond accordingly; for example, by adjusting scan parameters or by rejecting the subject. This technology is not yet available, however, and until then it will remain the responsibility of the system operators to ensure the safety of implant carrying patients in MRI.

View this article online at wileyonlinelibrary.com. DOI: 10.1002/jmri.27194

Received Nov 19, 2019, Accepted for publication Apr 30, 2020.

*Address reprint requests to: B.I., Physikalisch-Technische Bundesanstalt (PTB), Abbestr. 2-12, 10587 Berlin, Germany. E-mail: bernd.ittermann@ptb.de
Contract grant sponsor: EMPIR programme co-financed by the Participating States; Contract grant sponsor: European Union's Horizon 2020 research and innovation programme; Contract grant number: 17IND01 – MIMAS.

From the [1]Physikalisch-Technische Bundesanstalt (PTB), Braunschweig and Berlin, Germany; [2]Istituto Nazionale di Ricerca Metrologica, Torino, Italy; [3]ZMT Zurich MedTech AG, Zurich, Switzerland; and [4]Institute for Molecular Instrumentation and Imaging (i3M), Universidad Politécnica de Valencia (UPV), Valencia, Spain

Multiple fatal accidents have occurred with implant carriers in MRI,[4–6] mostly related to device malfunction. Severe injuries solely because of excessive device heating are also documented,[7–9] however, and for patients with implanted deep-brain-stimulators, RF heating is believed to be the biggest risk in MRI.[10,11] In phantom experiments, the temperature at the tip of a long wire increased by 75°C under RF exposure.[12]

The present article aims to summarize the state of knowledge (only) on implant-related heating in MRI. This restriction is not because the other aforementioned hazards would be less dangerous (the opposite is most certainly true) but because it is 1) omnipresent and 2) scientifically and practically the most challenging case for risk assessment.[13] Within the limited space of this article, we will focus on fully incorporated implants; interventional devices will not be covered, despite plentiful conceptual similarities.

In the following, the underlying physics of implant heating will be summarized. Also, the most relevant standardization documents in this field will be recapitulated, since they define how both scanners and implants are built and tested. Standards tell MR users what they can, or rather should not, expect from a device.

While this first part aims to provide a conceptual background at a level suited also for a general readership, the subsequent sections address mostly the active researchers in the field. Methods to assess and emerging concepts to actively mitigate implant-related hazards in MRI will be reviewed with a focus on recent developments. An extensive assessment of past developments that brought the field to where it stands today is not possible, within the present format. MR operators seeking practical advice about scanning or not scanning implant-carrying patients are kindly referred to the literature and continuously updated websites on this important subject.[6,14,15]

Physics of Implant Heating

MRI relies on two time-varying magnetic fields that differ in frequency and amplitude. The sinusoidal RF field B_1 is required to excite the spins to be imaged. Usually, it is generated by a volume transmit coil like the scanner's body coil or a dedicated transmit/receive head coil. The design target is a homogeneous B_1-field over most of the coil's geometrical volume. Amplitudes are in the 10 μT and frequencies in the 100-MHz regime. The second time-varying magnetic field is the gradient magnetic field B_G providing spatial encoding for image generation. The water-cooled gradient coils create $B_{0,z}$ gradients in all three directions. Design targets are linearly varying offset fields around the isocenter (where $B_G = 0$). Radially, B_G-fields are maximal at the bore; axially they have maxima around the end of the gradient coil, that is, at $|z| \approx 30 - 50$ cm. In modern clinical scanners, amplitudes reach the 10-mT regime in those areas. Gradient fields have base frequencies in the kilohertz regime but higher harmonics up to several 10 kHz often exist.

Faraday's law requires that all time-varying magnetic fields $B(t)$ are accompanied by electric fields $E(t)$, where $E \propto fB$ for sinusoidal $B(t)$ with frequency f. In an electrically conductive metallic implant with conductivity σ those E-fields drive so-called eddy currents with current densities $J = \sigma E$. This occurs also in biological tissue but is much more dramatic in metals, which typically—including "badly conducting" alloys—have $\sim 10^6$ times higher electrical conductivities. These induced currents have two effects, 1) due to ohmic losses, power $P \propto JE$ is locally deposited *inside* the implant, leading to a temperature increase with an initial slope of $dT/dt = P/C$, where C is the heat capacity of the exposed mass, and 2) secondary B- and E-fields are induced *around* the implant, which superimpose the incident E-field and modify the power deposition. Both effects can lead to tissue heating, but the mechanisms depend on frequency and thus are very different for gradients and RF.

RF-Induced Power Deposition in Tissue Around Implants

Under continuous RF exposure and without heat dissipation, the local tissue temperature would rise linearly in time with the absorbed RF power P_{RF} per exposed mass Δm, the so-called specific absorption rate (SAR):

$$\mathrm{SAR} \equiv \frac{\langle P_{RF} \rangle_t}{\Delta m} = \frac{\sigma \langle |E|^2 \rangle_t}{2\rho} \qquad (1)$$

where the angle brackets denote temporal averaging. Electrical conductivity σ and mass density ρ are tissue parameters, E depends on MRI hardware and software, that is transmit coil and sequence. SAR is a local quantity since all parameters are position-dependent and Eq. (1) holds with or without an implant being present.

In a periodic MR sequence, $\langle P_{RF} \rangle_t$ in Eq. (1) is given by the sum of all pulse energies $\int P_{RF}\, dt$ divided by the repetition time (TR). Consequently, sequences with short TR and a high density of high-power pulses have increased SAR values. Time-averaged SAR can be modified and limited to safe exposure levels; for example, by reducing the flip angle and thus the power per RF pulse, and/or by extending TR and thus the mean time between RF pulses.

RF currents at $f \sim 100$ MHz in metals are restricted to a thin surface layer of ~ 100 μm by the laws of electrodynamics ("skin effect"). The mass of directly heated implant material remains too small, therefore, to affect the neighboring tissue noticeably. The current-induced secondary E-field (the "scattered field") around the implant becomes highly relevant, however, as it can vastly exceed the primary "background" E-field in critical locations. RF currents induced directly in tissue by the scattered E-field are the dominant effect for

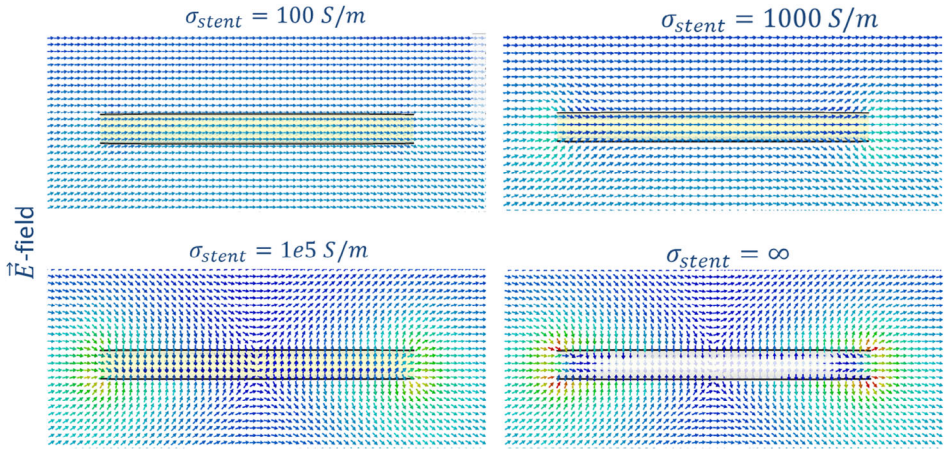

FIGURE 1: Simulated electric-field distribution of a stent with varying conductivity. For highly conductive material such as metals, a scattered field is induced by the current in the stent, which exceeds the incident electric field and creates *E*-field (and SAR) hotspots at the stent tips.

implant-related RF heating (Fig. 1). In particular one-dimensional implants tend to exhibit the so-called antenna effect; that is, a pronounced maximum of the scattered *E*-field at their distal end, whose intensity peaks when the electrical length of the implant is in the range of one-quarter to one-half of the RF wavelength in tissue.[16] The electromagnetic energy of the background field is then most effectively converted into implant current and corresponding scattered field.

Gradient-Induced Power Deposition in Implants

In contrast to the RF case, secondary *E*-fields and the direct induction of currents *in tissue* are both negligible for gradient switching at kilohertz frequencies. Switched gradients can heat up the metallic implant itself, however, via eddy currents. These currents and the associated power deposition are confined to the metal, but thermal energy diffuses subsequently into adjacent tissues. Such confined eddy-current loops are intrinsically limited in small or one-dimensional implants (eg, screws or leads), but possibly significant in implants with a large cross-section (eg, orthopedic prostheses), where large, low-resistance closed current paths exist.[17,18]

Eddy currents inside a sphere, for example, the ball end of a hip implant, encircle the switched gradient field B_G and their density is[18]:

$$J = \frac{B_G}{\mu_0}\frac{3k^2R}{2\sin(kR)}\left[\frac{\sin(kr)}{(kr)^2} - \frac{\cos(kr)}{kr}\right]\sin\theta \qquad (2)$$

in a generic radial position r, with magnetic permeability of vacuum μ_0, colatitude θ with respect to the direction of B_G, assumed to be uniform, and $k^2 = -2\pi i f\mu_0\sigma$,where $i = \sqrt{-1}$. Equation (2) considers the skin effect and that eddy currents produce a secondary magnetic field perturbing the applied one. In the equatorial plane and for low k, that is low $f\sigma$, Eq. (2) and simplifies to:

$$J = \sigma f B_G \pi r \qquad (3a)$$

Equations (2) and (3a) refer to the (complex) amplitudes of (rarely occurring) sinusoidal gradients with frequency f. For generic time-signals $B_G(t)$, Eq. (3a) can be expressed as:

$$J(t) = \frac{1}{2}\sigma r\frac{dB_G(t)}{dt} \qquad (3b)$$

A broad variety of gradient waveforms exists but trapezoidal pulses with linear B_G ramps and flat tops are the most common. Only the ramps create eddy currents then; the flat sections do not contribute. Under the simplifying assumptions of Eq. (3b), the induced current density scales with implant conductivity, the change rate of B_G, and the radius r of the current loop. The total heating power of those currents depends on the square of the current density.

For a given implant, gradient heating is maximal, when the implant is positioned in the aforementioned locations of highest B_G, when the gradients are ramped at the highest available slew rate, and when the sequences are run with a high "slew percentage," that is a high fraction of ramp time during TR. The gradient strength itself is only indirectly a factor, insofar as higher gradients need longer ramp times to reach them.

Few studies on gradient-induced implant heating exist. Earlier ones did not find significant temperature elevations,[19,20] but did not systematically investigate critical scenarios as described in the previous paragraph. More recent work showed that gradient heating of hip prostheses can increase the temperature in adjacent tissue by several degrees using a manufacturer-provided "gradient aggressive" sequence, in the aforementioned sense, on a clinical scanner.[17,21–23] See Fig. 2 and Table 1 for an example. Very close agreement between experimental findings and computations indicate that the effects are well understood.[23]

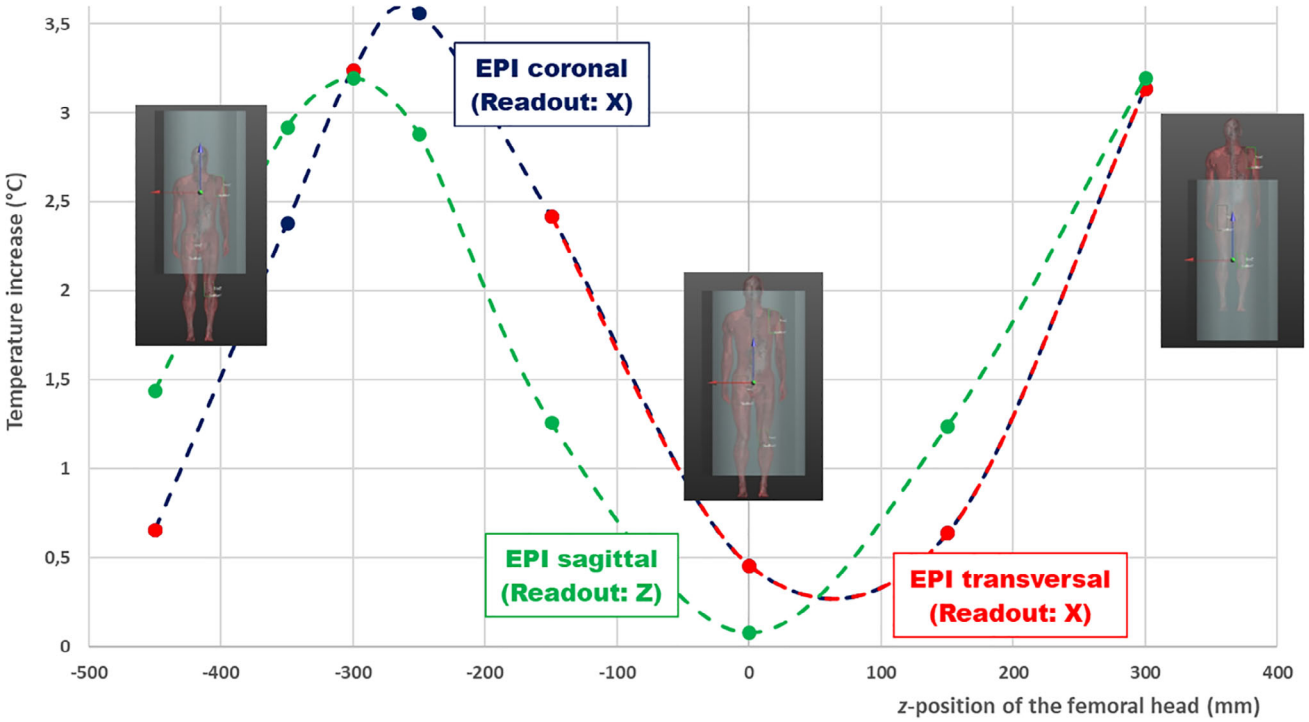

FIGURE 2: Maximum gradient-induced heating of a hip implant made of CoCrMo alloy after 12 minutes of continuous exposure to an EPI sequence performed by standard gradient coils for different readout directions and at different longitudinal positions of the body. The results refer to a gradient strengths of 20mT/m, a TR = 43 msec, and a readout slew rate of 168 (T/m)/s for a relatively short gradient-coil assembly.

From Power Deposition to Heating to Tissue Damage

So far, only implant-related changes in the power deposition were discussed but the hazards are excessive tissue *temperatures*, and temperature is established by the balance of heating and cooling. Implant heating is a local phenomenon and the most widely used description in this context is the Pennes Bioheat Equation (PBE)[24]:

$$c_t \frac{dT_t}{dt} = \nabla \cdot \left(\frac{k_t}{\rho_t} \nabla T_t \right) + \rho_b c_b w_t (T_b - T_t) + Q_m + Q_{ext} \quad (4)$$

Parameters are specific heat capacity c (W s kg^{-1} K^{-1}), thermal conductivity k (W m^{-1} K^{-1}), mass density ρ (kg m^{-3}), and blood perfusion w (m^3 s^{-1} kg^{-1}). The subscripts t and b refer to tissue and (arterial) blood, respectively. Tissue temperature change on the left is expressed as the balance of heat diffusion, perfusion cooling, metabolic heat Q_m (W kg^{-1}), and external heat Q_{ext} (W kg^{-1}), such as SAR. Equilibrium (dT_t/dt = 0) is reached when the terms on the right-hand side compensate each other. PBE is not a fundamental law and makes a number of questionable assumptions (the blood pool as infinite heat sink, isotropic thermal conduction, inadequate perfusion model, absence of thermoregulation, etc.). Still, it appears to be working remarkably well in predicting tissue temperatures (see, eg, Ref. 25 for an extended discussion).

Thermal modeling is indispensable to assess gradient-heating-related hazards since the deposited power reaches the tissues only via thermal diffusion. But also for RF heating, where the existing regulations only impose limits on SAR, it is highly advisable. The tissue parameters k_t, w_t, and Q_m in Eq. (4) can vary by orders of magnitude between tissue types.[26] Even a uniform external power deposition would therefore result in a nonuniform distribution of equilibrium temperatures in the body. Equivalently, it can be said that for a nonuniform SAR distribution the temperature hotspots will not normally coincide with the SAR hotspots.[27] This discrepancy can be further enhanced by the high *thermal* conductivity of metallic implants. This reduces temperature differences along the implant and tends to smear out local hotspots.

For a conclusive safety assessment, however, even a realistic temperature distribution is not yet sufficient, as tissue types vary not only in cooling properties but also in temperature resilience: 10 minutes at 45°C is not much of a problem for skin but it is for brain matter.[28] *Thermal dose* safety concepts, considering the applied temperature over time individually for each tissue type, account for this variation and arguably represent the best that can be done today. The best known example is the "*Cumulative Equivalent Minutes at 43°C*" (CEM43) approach.[28–31] This is beyond the scope of

TABLE 1. Maximum Temperature Elevation ΔT_{max} vs. Position z of the Hip Joint in the Scanner After 12 Minutes of Continuous Exposure to a Coronal EPI Sequence With Frequency Encoding Along the x-axis, for a CoCrMo Prosthesis

z (mm)	−450	−350	−300	−250	−150	0	150	300
ΔT_{max} (°C)	0.66	2.38	3.24	3.56	2.42	0.46	0.64	3.14

Simulation data from Ref. 23. For $z < 0$, $z = 0$, and $z > 0$, the upper body, pelvis, and lower limbs, respectively, are in the imaging position. See also Fig. 2.

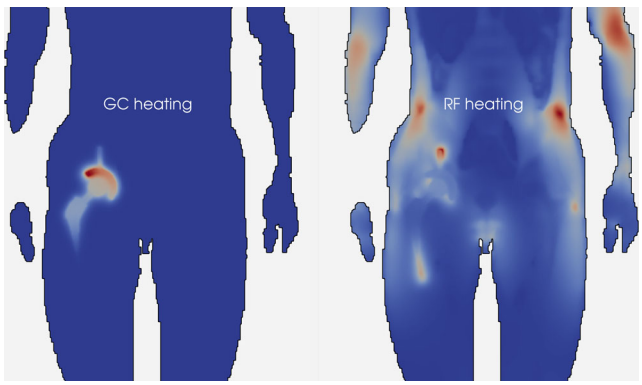

FIGURE 3: Numerical simulations of the same voxel model (male adult with unilateral hip prostheses) illustrating the different distributions of the temperature elevations resulting from gradient heating (left) vs. RF heating (right). Gradient heating is confined to the immediate vicinity of the implant and effective only in extended cross-sections (here the acetabular cup). RF heating can create hotspots everywhere in the body. The implant-related contribution of RF heating is most prominent at pointed elements as the tip of the femoral stem or the screw protruding from the acetabular cup. No absolute scales are given since the exposure conditions cannot be compared.

this review, however; the present standard is—literally—still SAR.

RF Heating vs. Gradient Heating

As mentioned, RF-induced currents are confined to a thin surface layer by the skin effect, while the low-frequency gradient currents fill almost the whole volume. Compared to RF fields, gradient switching has lower frequency content ($<10^5$ Hz vs. $\sim 10^8$ Hz), but higher magnitude ($\sim$10 mT vs. $\sim$10 μT). The combined effect is that in bulky metallic objects, switched gradients can deposit much more power than RF.[18] In a nonmagnetic sphere (radius R = 2 cm, σ = 1 MS/m, similar to the femoral head of a hip implant made of CoCrMo alloy), the power deposition by a gradient field of B_G = 6 mT at f = 1 kHz is about 900 mW, compared to 8 mW for an RF field of 10 μT at 64 MHz (B_0 = 1.5T) and 10 mW at 128 MHz (B_0 = 3T).

The effects of implant and sequence parameters on implant-related heating via RF and gradient switching are compared in Table 2. A graphical illustration of the qualitative differences is given in Fig. 3.

Standards and Guidelines

When it comes to the safety of medical devices, the importance of standards cannot be overestimated. No product makes it to the market unless it conforms to the applicable standards. These documents define, therefore, how devices are built and tested. They tell users what they can, or better, should not expect from a given device.

A set of international standards was established over the last decades covering implant safety in MRI,[33] supplemented by recommendations from governmental agencies.[34,35] All refer to the international MR-safety standard IEC 60601–2-33, first established in 1995.[36] Below, we summarize the three most relevant standards concerning implant-related heating in the MR environment, namely, ASTM F2182,[37] IEC 60601–2-33,[36] and ISO/TS 10974.[38] Note, however, that the instructions of use provided by the scanner manufacturer may be more restrictive than the currently applicable standard. These instructions are legally relevant, as not following them constitutes *off-label use*, with potentially severe liability implications for the MRI operator.

All three standards adopt a scheme from ASTM F2503,[39] where implants are labeled as either *MR unsafe* ("an item that is known to pose hazards in all MRI environments"), *MR conditional* ("an item that has been demonstrated to pose no known hazards in a specified MRI environment with specified conditions of use"), or *MR safe* ("an item that poses no known hazards in all MRI environments"). Note that metallic items can always exert Lenz forces and create image artifacts, which are considered diagnostic hazards,[40] and hence are never *MR safe* in this terminology. This labeling is the responsibility of the implant manufacturer who defines the conditions for safe use in MRI.

ASTM F2182

The ASTM standard F2182[37] is fully designated to RF-related implant heating. It provides the implant manufacturer

TABLE 2. Qualitative Comparison of RF and Gradient Heating in Terms of Implant and Sequence Parameters

Parameter	RF heating	Gradient heating
Implant size	Most critical: lengths around quarter to half the RF wavelength in tissue.	Most critical: bulky implants
Implant shape	Most critical: one-dimensional; pointed ends; multiple implants with short gaps between them.	Most critical: large cross-sections
Implant material	Electrical conductivity is less relevant, higher thermal conductivity reduces temperature hotspots.	Higher electrical conductivity gives higher eddy currents. For example. CoCrMo alloy creates ~60% more gradient heating than Ti-6Al-4 V.[18] Thermal conductivity is less relevant.
Implant position	Most critical: Regions of highest background *E*-field.[32] In a conventional body coil this field increases radially with distance from the coil axis (where it vanishes). Axially, the field is uniformly high within the footprint of the coil; substantial field tails beyond the end of the coil can exist.	Not critical: isocenter. Critical: Locations in the bore where B_G-fields are highest, which is towards the ends of the gradient coil, that is, outside the imaging region (Fig. 2). Radially, B_G increases monotonically with distance from the magnet axis; axially, a maximum is reached at $\|z\| \approx 30 - 50$ cm from the isocenter, depending on the gradient coil (see Table 1 for a specific example).
Implant orientation	Most critical: implant aligned with the background *E*-field vector (ie, parallel to the magnet axis for conventional body coils)	Most critical: large implant cross-section perpendicular to the direction of switched B_G-fields with high amplitudes.
MR-sequence parameters	Most critical: fast sequences with high density of large flip-angle RF pulses, for example, turbo spin echo. Higher (local and whole-body) SAR as indicated by the scanner corresponds to more critical sequences but the readings do not account for the implant and different exposure conditions (scanner, RF coil, subject, position, etc.) cannot be compared.[3]	Most critical: fast sequences with high slew rates and high slew percentage, for example, echo-planar imaging. Critical conditions are not indicated by the scanner.

with well-defined procedures and materials for in vitro heating tests of their devices. The standard itself defines no pass-or-fail criteria; the test results are sent to and evaluated by a competent authority, most notably the US Food and Drug Administration, for a decision on the conditionality of the implant for MRI. There are other related ASTM standards (ASTM F2052, F2119, F2213, and F2503) which are outside the scope of this review.

ASTM F2182 describes in detail a test procedure where the implant under test is embedded in a phantom setup and exposed to a whole-body SAR of 2 W/kg by using either a 1.5T or 3T MRI scanner or a suitable benchtop system reproducing the RF fields from a body coil in circular-polarized (CP) mode. For 15 minutes the temperature is monitored, and local SAR is determined calometrically. By repeating measurement with the implant removed, the baseline temperature rise is also measured, and the implant-related temperature rise can be determined.

The scope of ASTM F2182 is limited to passive implants completely inside the body. Similar methods as described in ASTM F2182 can be applied, however, for devices penetrating the body's surface; for example, catheters. Procedures described in ASTM F2182 are also appropriate to perform validation experiments as required by ISO/TS 10974.

IEC 60601–2-33

The IEC 60601–2-33 standard[36] is the most relevant safety and performance standard for MRI. It provides MRI scanner manufacturers with a comprehensive set of criteria and limits, thus allowing them to self-declare conformity if all requirements are met. This standard is all about the scanner in general; implant safety is only one of many topics.

According to IEC 60601–2-33, the risk of RF-induced heating of an MR-conditional device should be assessed in terms of the root-mean-square (RMS) averaged $B^+_{1,\mathrm{RMS}}$:

$$B^+_{1,\mathrm{RMS}} = \sqrt{\int_0^{t_x} \frac{\left(B_1^+(t)\right)^2 dt}{t_x}} \qquad (5)$$

with an averaging period t_x = 10 s. From prescan flip-angle measurements, the absolute value of B_1^+ can be determined, making $B^+_{1,\mathrm{RMS}}$ a reliably calibrated quantity when averaged over a proper region of interest in a central axial slice. $B^+_{1,\mathrm{RMS}}$ is typically calibrated by the MR system and its values should be displayed by the MR software. It is important to note, however, that implant heating is related to the total B_1 (all three vector components), not just B_1^+, and the standard gives some guidance to estimate the uncertainties when using $B^+_{1,\mathrm{RMS}}$. This quantity is a much more consistent approach to assess RF-induced implant heating than whole-body SAR, which was the reference in the past. In contrast to whole-body SAR, $B^+_{1,\mathrm{RMS}}$ is independent of the patient and calculated consistently by different MRI manufacturers.

In the latest version of IEC 60601–2-33, the so-called fixed-parameter option (FPO) was introduced for 1.5T systems (FPO:B), which specifically addresses the scanning of implant carriers. In FPO:B mode, both the RF and the gradient outputs are restricted, and the scanner manufacturer guarantees that specified maximum values are nowhere exceeded, within a defined volume in the bore. Important FPO:B limit values are $B^+_{1,\mathrm{RMS}}$ = 3.2 µT and $|dB_G/dt|_{\mathrm{RMS}}$ = 56 T/s, where:

$$\left|\frac{dB_G}{dt}\right|_{\mathrm{RMS}} = \sqrt{\int_0^{t_x} \frac{\left(\left|\frac{dB_G}{dt}\right|\right)^2 d\tau}{t_x}} \qquad (6)$$

is the time-averaged temporal derivative of the gradient field. The latter limit relates to gradient-induced implant heating but was introduced chiefly to protect the device from damage. Note that the FPO:B limits do not by themselves define "safe scan" conditions. The FPO rationale is that the scanner manufacturer guarantees that those field limits are kept, such that implant manufacturers can design and test their devices accordingly. Only the combination, a scanner in FPO mode and an FPO-approved device, would then establish a safe setting. The problem of FPO is that a single set of field limits must suffice for a huge variety of medical implants. Up to now, medical implants labeled as MR conditional with respect to FPO:B are very rare.

ISO 10974

The ISO/TS 10974:2018(E)[38] is the first comprehensive standardization document on active implantable medical devices (AIMD) in an MRI context. Its purpose is to provide manufacturers of active implants with defined procedures and methods to assess the MRI safety of their devices. Conceptually, it is the active-implants counterpart of ASTM F2182, therefore, which covers only passive implants. In its current version, the scope is restricted to 1.5T scanners with a cylindrical bore and body coil excitation. With respect to RF heating, the standard deals with implant-related effects only, and not with possible background-SAR hotspots elsewhere in the body (which are covered by IEC 60601–2-33).

To determine the RF-power deposition, a four-tiered approach is prescribed (Fig. 4). The tiers represent different levels of complexity and accuracy. Lower levels are synonymous with lower accuracy and larger safety margins that need to be applied. Tier 1 does not require electromagnetic modeling. Tier 2 uses simulated human RF exposures to "determine the electric field in the implant volume of interest." Tiers 1 and 2 are restricted to electrically short AIMDs, since phase effects are not included. For Tier 3 an equivalent electromagnetic model of the AIMD is required to determine the transfer function.[41] Tier 4 assesses the AIMD electromagnetic model within anatomical models for relevant RF-exposure conditions. Except for very simple implants, the Tier 4

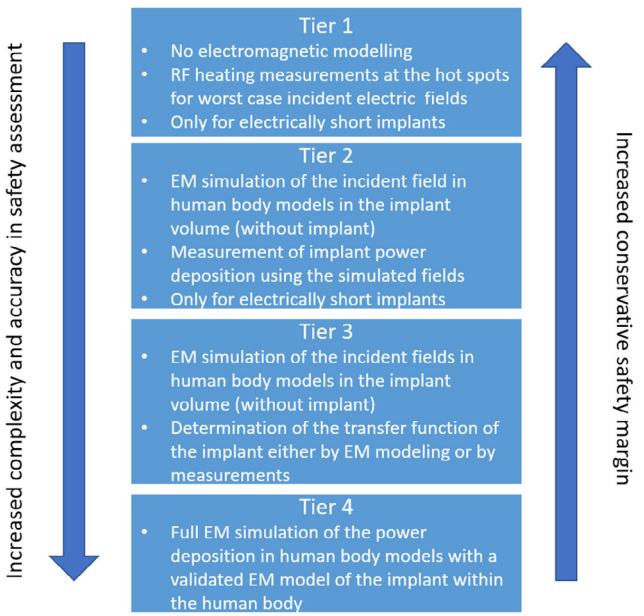

FIGURE 4: Schematic of the 4-Tier approach for implant-safety assessments in the ISO/TS 10974 standard.[38] Each level increases the complexity of the simulations and/or testing methods, but at the same time increases the accuracy and decreases the overestimation of RF-induced heating, which allows for safe, but less conservative safety margins.

approach is challenging, using state-of-the-art computational capabilities.

Detailed requirements are given on how measurements should be performed to validate the simulations and ISO/TS 10974 also deals with gradient-induced device heating in a tiered approach.

Methods to Assess Implant Safety

Simplifications

Long, 1D-like implants, for example, pacemaker leads, collect RF over their entire length, which makes them potentially hazardous and simultaneously defies simplifying assumptions like a constant *E*-field, in magnitude and phase, over the whole implant. Their structural details, for example, a finely wound helix or multiple electrodes, and steep field gradients near the implant call for a high mesh resolution but the simulation space, defined by the body coil, remains large. To aggravate the problem, the trajectories for long leads are not well defined, and a variety of different pathways need to be investigated. Numerical simplification approaches exist and are widely used; for example, the Huygens box concept[42] where a high-resolution simulation of the implant region is embedded in lower-resolution simulation of the rest of the body. For a discussion of the pros and cons of such procedures the reader is referred to more specialized reviews on numerical techniques.[43]

To simplify the geometry, helices are often modeled as straight wires plus lumped elements to account for their inductance or stents as cylinders, ignoring their complex wire-mesh structure.[44,45] Despite these efforts, full Tier 4 simulations are not yet feasible with normal computational resources and Tier 3 represents the actual state-of-the-art. There, first the full-scale native problem, that is, a numerical body model without implant in an MRI scanner, is computed at an appropriate resolution providing the spatial distribution of the unperturbed background *E*-field. This part may be repeated for different body models, positions, postures, or transmit coils, resulting in a library of background fields. In a second step, the electrodynamic response of the metallic implant to that background field is computed. Frequently, this is expressed as the "scattered field," that is, the difference between total *E*-field with implant and background field.

The critical spot of a wire-like implant is always at the distal tip and a frequent simplification therefore is to ignore all other locations. The scattered field at the tip can be derived from the background-field distribution along the implant trajectory. A first step in that direction was the definition of a "safety index" as a metric to characterize 1D-implants.[46] Later, this was succeeded by the introduction of the transfer function (TF),[41] the most widely-used approach to assess the MR safety of 1D implants today. To determine the scattered *E*-field at some reference position $\vec{r}$ in tissue,

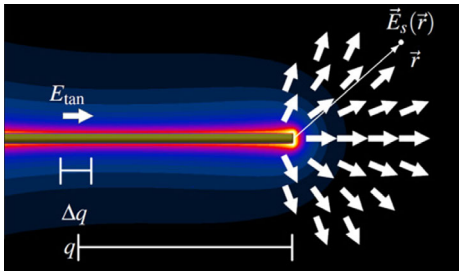

FIGURE 5: Graphical representation of the transfer function introduced by Park et al 2007.[41] A piece-wise excitation with an incident tangential electric field E_{tan} induces a scattered electric field $\vec{E}_S(\vec{r})$ at the tip of a 1D implant (figure from Tokaya et al, 2017, Ref. 47). The length coordinate *q* in this figure is denoted $\hat{z}$ in the present article (see Eq. 7).

close to the tip, one needs to know the response $E_s(\vec{r})$ of the *E*-field at the reference point to a unit tangential *E*-field applied somewhere along the implant (Fig. 5). The latter location is uniquely identified by a scalar coordinate $\hat{z}$, measuring its distance from the tip along the implant trajectory. This response can be expressed as a complex weight function $S(\hat{z},\vec{r})$ and the desired "scattered" field $E_s(\vec{r})$ can then be obtained by integrating the weighted tangential background field $E_{tan}(\hat{z})$ along the wire:

$$\vec{E}_s(\vec{r}) = \vec{F}_{tip}(\vec{r}) \int_0^L S(\hat{z}) E_{tan}(\hat{z}) d\hat{z} \qquad (7)$$

The normalized, dimensionless function $\vec{F}_{\text{tip}}(\vec{r})$ describes the spatial distribution of the scattered *E*-field around the tip and is assumed to be independent of how the implant was excited. The problem is thus broken down to two independent steps, namely, to determine 1) the background *E*-field without implant, and 2) the transfer function $S(\hat{z})$ of the implant. The former means a state-of-the-art EMF simulation; the latter can be achieved either by simulations or experimentally. TF is a normalized, complex function, determining how various elementary RF currents induced along the length of the implant superimpose at the tip. In this picture, the TF phase describes the propagation and the TF magnitude the attenuation of an RF current along the implant. In the simplest case, the TF phase would be a linear function of the distance from the tip. The *E*-field "collected" within half a certain distance from the tip would then increase the scattered field around the tip, while contributions from beyond that point would decrease it again (Fig. 6). For longer distances, attenuation dampens the interference pattern, but a critical "resonance length" of about half the current wavelength persists. This wavelength, and hence the TF, depend on the dielectric parameters of the tissue and possibly an insulation surrounding the implant. The TF of an implant depends on its environment, therefore, but for simplicity this fact is often ignored. For unfavorable phase distributions of

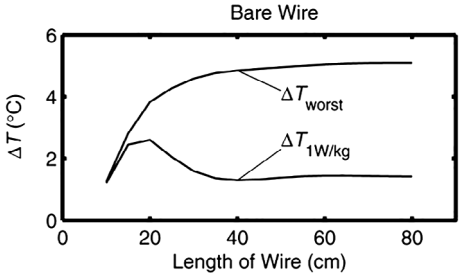

FIGURE 6: Temperature increase at the tip of a bare wire as a function of wire length for RF exposure at 64 MHz. For a uniform phase distribution, the temperature increase ($\Delta T_{1W/kg}$) shows a maximum at a "resonance length" of roughly half the RF wavelength in the phantom medium. If the phase distribution is nonuniform over the implant (ΔT_{worst} = temperature increase for a worst-case phase distribution), which is often the case for very long implants, the tip temperature can increase even above the resonant length of the wire (figure from Park et al, 2007, Ref. 41).

the background *E*-field the tip heating can significantly exceed even the values for the resonant length (Fig. 6).

The TF can be determined by measuring or calculating the scattered *E*-field at some reference point $\vec{r}$ close to the tip when the implant is exposed to a piece-wise excitation by a unity tangential *E*-field. In simulations, this can be approximated artificially by a short boxcar function[41] or as the *E*-field between two parallel metallic plates in close proximity.[47] Experimentally, for example, short toroid coils[48] or coaxial cables with a few millimeters of bare inner conductor[49] can be used.

An important advancement to reduce the multitude of piece-wise excitations and measurements (and/or simulations) to a single excitation is based on the principle of reciprocity.[50] Injecting a unit current at its tip, the TF is represented by the current distribution along the implant and several experimental strategies were proposed to determine this current.[49,51]

Numerical Simulations

The numerical assessment of implant heating in the MRI scanner involves a whole chain of exposure assessments, which can broadly be categorized into 1) 3D-CAD models of RF or gradient coil, implant, and patient; 2) the electromagnetic simulation including dielectric properties of all involved tissues and electrical elements; and 3) the thermal simulation along with thermal and physiological tissue parameters.

Here we focus on the implant-related aspects of simulations. A more detailed overview of electromagnetic-simulation techniques in an MR-safety context in general can be found, for example, elsewhere.[52]

REALISTIC SIMULATION AND BODY MODELS. If the 3D-CAD model of an implant cannot be obtained from the manufacturer, an electrically equivalent simulation model could be created from the actual implant, based on its geometry, composition, and size. RF and gradient coils are integral parts of the MR scanner and their actual design is more difficult to create. However, RF-field measurements can be utilized to give a good estimate about the design, length, and diameter of commercial RF body-coils.[53,54] Regularly at 7T, but occasionally at lower field strengths too, local transmit-receive coils are used; for example, for knee or head scans. In such a case, implant-safety assessments are only possible if the RF fields or the RF-coil model are known.[55,56] It is important to apply the correct coil-driving conditions. Body coils of 1.5T scanners typically apply only the CP mode, whereas at 3T and above RF shimming is common to counteract B_1^+ inhomogeneities.[57–59]

The distribution of the gradient magnetic field B_G can be derived from quasistatic field measurements or manufacture-provided field maps, if available.

Regarding numerical body models, a wide range is available with increasing resolution and quality.[60–62] An extensive review on body models for electromagnetic simulations can be found in Ref. 63.

The dielectric properties of human tissues can be assigned according to literature values. Reference 64 is the pioneering article in this respect, while the wealth of today's knowledge in this field is conveniently compiled in Ref. 26.

ELECTROMAGNETIC SIMULATION TECHNIQUES. ***RF Fields and Currents.*** There are several simulation techniques in computational electromagnetics, each with advantages and weaknesses. For birdcage coils, the method of moments (MOM; also called boundary element method, BEM) or the finite elements method (FEM) may be the best choice, as they can treat curved geometrical objects more accurately than other techniques. However, when complex anatomical models or structures are involved, the simulation space can easily reach dimensions of 100 million voxels (3D pixels) or more, which is most efficiently handled by the finite-difference time-domain (FDTD) technique. Calculations can be parallelized on graphics processors, thus shortening simulation times by factors >100. The simulation output contains the induced *E*-field distribution in the patient for a given exposure scenario and can be expressed as SAR maps, which are subjected to different averaging volumes. The most important of which are the whole-body average SAR and the local SAR averaged over 10 g of tissue.[36] For implants, there is an ongoing discussion whether smaller averaging masses should be used to assess temperature and thermal dose more correctly.[44,65,66]

The exposure condition in the simulation model such as linearly polarized, CP, or RF shimming, is important and needs to match reality, since it determines the background *E*-field distribution responsible for the RF-induced implant heating. With state-of-the-art EM modeling, satisfactory

agreement (for the given purpose) with phantom measurements can be obtained and (standard) uncertainties in the range of 10–15%[67] should be achieved for local-SAR values, as the dielectric properties of the tissues are only minimally affected by the physiological response.

Gradient Fields and Induced Currents. Most articles dealing with the simulations of gradient-induced heating of bulky implants adopt the hybrid FEM/BEM frequency-domain formulation described in Ref. 21. Such a formulation applies to nonmagnetic metallic implants and, at the frequencies of interest, assumes that the current density induced inside bulky implants is much higher than in the surrounding tissues, thus limiting the electromagnetic problem to the implant volume. To simulate a gradient sequence realistically, the harmonic solutions are moved back to the time domain, where they are properly combined to follow the actual waveforms of the three gradient coils.

THERMAL SIMULATIONS. The power-density distribution from electromagnetic simulations can be used as input for thermal simulations (Fig. 7). Steady-state solvers can be used when only absolute equilibrium temperatures are of interest. To simulate temperature increase vs. time, more complex transient time-domain solvers are required. As previously stated, the PBE[24] is presumably the most widely used formulation and most commercial software to calculate tissue temperatures employ PBE or amended variants; for example, with thermoregulation included (ie, temperature-dependent tissue parameters). It performs well for the given exposure scenarios but is a heatsink model assuming stable core temperatures. If a core temperature increase must be considered, the PBE can be enhanced by a variable blood-temperature formulation. Other aspects remain neglected, however, such as anisotropic heat-flux or blood-temperature variations along the vessel. For the latter, the impact of the thermal vasculature could be investigated based on a model coupling 1D convective vascular-tree thermal simulations with 3D thermal modeling.[68] While the PBE assumes that the arterial inflow to tissue is still at core temperature, such discrete-vasculature (DIVA) models[69] acknowledge the flow directionality and the gradual thermalization of blood along the (arterial) vascular tree. Other formulations are also being used such as the generic bioheat transfer model.[70]

The total uncertainty for modeling the relatively high local-temperature increase in MRI is about 20–30% (standard uncertainty),[31] with the largest contributions from tissue perfusion and thermoregulatory response.

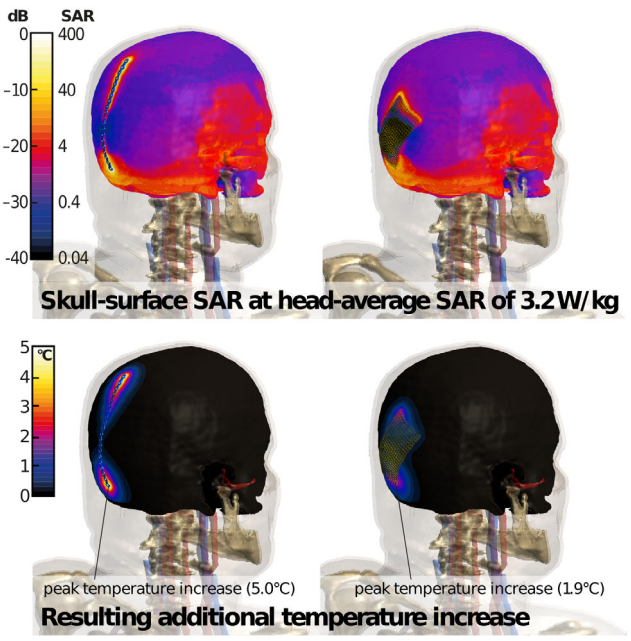

FIGURE 7: Electromagnetic and temperature modeling and simulations of two different implant types positioned on the skull of a human body model. SAR can be calculated based on the power deposition and used in the temperature simulations to determine the peak temperature increase at the implant for a given input power to the RF coil.

TOWARDS SUBJECT SPECIFIC MODELS: MORPHING AND IMAGE REGISTRATION. Sophisticated EM modeling can be performed on virtual body models, but these models never represent the true patient geometry. Personalized exposure evaluations might allow reducing the necessary safety margins for the majority of the patient population, and consequently permit faster and safer MR scans; for example, a dynamic adaptation of exposure limits based on the patient's BMI or body cross-section.[67] We will briefly discuss two methods, a physics-based morphing and a 3D image-registration approach.

A physics-based morphing technique can be applied on existing anatomical models via constrained biomechanical FEM simulations, where the body is treated as a hyperelastic material.[71,72] The tissue deformation is constrained by the proximity of rigid bones and regularized by the presence of surrounding soft tissue. This allows regional shrinkage or expansion of certain tissues (eg, fat, muscle) to investigate the effect of different tissue distributions. A look-up table can be generated, where the actual patient would be matched to the closest morphing variant of an anatomical model. Precomputed exposure data would serve as a coarse personalized estimate.

If a certain target anatomy of the actual patient is aimed for in higher detail, a 3D image registration is better suited to capture the actual skeletal anatomy and posture. Sparse (eg, cross-sectional) pilot-scan images of the patient could be used as input for the nonrigid registration approach[73–75] to map the numerical phantom to the patient-specific anatomy. The resulting 3D-registered derivative can then be used to compute the exposure estimation on-the-fly.

As of today, personalized EM simulations are not yet in widespread use.

Measurements

Measurement procedures for in vitro model validation are well described in ISO/TS 10974.[38]

Assessments can be done at points of interest near the implant, by measuring either 1) electromagnetic-field quantities using time-domain sensors, or 2) root mean square (rms) quantities like voltage or temperature. Fiberoptic temperature probes are the most widely used sensors for safety assessments in MRI. They use a nonconducting transmission medium and are nonmagnetic, preventing RF coupling and enabling an application inside an MR scanner. For accurate assessment of temperatures, probe positioning is crucial. For example, for a peak temperature of 10°C a 1°C change can be observed over less than 250 μm.[76]

Time-domain probes yield information on amplitudes and phases of field quantities, which is necessary, for example, for TF measurements.[49] For in situ applications in the scanner, the field probes must be nonmagnetic and must not generate static magnetic fields, for example, by internal DC currents. Examples for in situ RF-current measurements on implanted wires using optical fibers for signal transfer can be found in Refs. 12,77.

Another approach to perform in situ measurements, especially in active devices, is the use of built-in sensors. Due to the lack of a phase reference, this appears to be limited to rms measurements, so far, but this issue may be resolved in the near future using state-of-the-art electronics. In a proof-of-principle study[78] it was shown that the temperature at the tip of an implanted pacemaker surrogate can be reliably measured during in vivo MRI using wireless data transfer.

In Vivo Assessments of Implant Safety

Recently, methods have been investigated to assess implant safety in vivo. This methodology, if further developed and validated, would enable patient-specific safety assessments of implanted devices.

NON-MRI-BASED METHODS. A metallic implant with strong coupling to the RF coil causes significant impedance changes. These can be measured, via the coil's current distribution or scattering (S) parameters, and related to the induced implant current strengths and even the location of the implant if a multichannel transmission system is used[79–81] (Fig. 8). Such an "implant detector" at the MR-system level would solve many problems, only it will be very difficult to ensure that every hazardous implant is detected.

Another method to determine potential RF-induced heating in vivo independently of prior simulations is the use of integrated temperature sensors in the implant at locations where a maximum temperature increase is expected[78,82] or

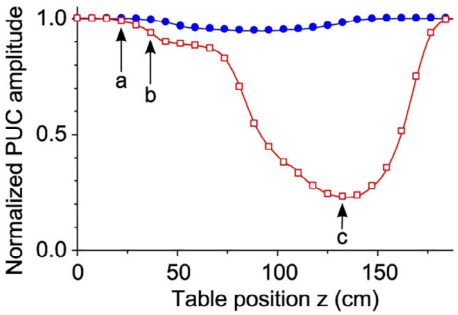

FIGURE 8: Normalized signal from a pick-up coil (PUC) as a measure of the current in one element of a parallel-transmit (pTx) coil array when a phantom with (red) and without (blue) a disconnected pacemaker lead inside is moved through the scanner. Decreased pick-up signal reflects increased coupling of the load (phantom plus implant) to the RF-coil element. Temperature measurements at table positions (a) and (b) showed no or negligible heating, respectively, while a temperature increase of 43.7 K within 30 seconds was observed at position (c), indicating a strong correlation between the detected coil-implant coupling and the heating effect (figure from Graesslin et al, 2013, Ref. 79).

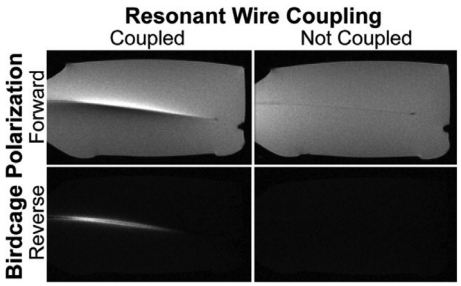

FIGURE 9: MR image artifacts associated with induced current on a wire. If the wire is not coupled to the RF fields, only small signal changes indicate the location of the wire. If the wire is coupled to the transmitted RF, the current induced on the wire alters the B_1^+ distribution in its vicinity and leads to severe signal changes, resulting in bright and dark spots along the wire. Reversing the polarization of the birdcage RF coil shows only the wire currents, while the background signal disappears (figure from Overall et al, 2010, Ref. 88).

the utilization of the thermo-acoustic effect.[83,84] The latter exploits the pressure waves that a sudden temperature increase inevitably generates and which can be detected by sensitive acoustic receivers. It has been shown in a proof-of-concept study that this ultrasound signal can be used to detect RF-induced heating of a lead tip and therefore could be utilized in a prescan procedure.[84] Translating such ultrasound-based systems to a robust clinical in vivo application is challenging, however (eg, receiver size and positioning, movement, acoustic window, signal-to-noise ratio [SNR], quantified measurements etc.), and still needs to be demonstrated.

MRI-BASED METHODS. The MR scanner itself is a versatile machine and several publications demonstrated that it can be utilized for noninvasive implant-safety assessment and

monitoring in vivo. This is ongoing research, however, and not yet routinely available.

For elongated implants, tip heating is related to the RF eddy currents in the implant,[85] which then induce a new $B_{1,ind}$-field altering the total B_1^+ . Consequently, tip heating can be estimated by MRI-based measurements of B_1^+ around the implant[86,87] (Fig. 9). If $B_{1,ind}$ has a z-component, it will also shift the RF phase.[89]

Implant-related image B_1 effects can also be translated to direct measurements of the induced RF current in the implant. This may appear as a detour, as ultimately the quantity of interest is temperature and implant current only a surrogate. The advantage of current measurements is their sensitivity. In principle, relatively small and harmless implant currents are detectable in vivo, while a measurable temperature rise is typically already hazardous for the patient. Often, model assumptions like a perfect quadrature excitation or simplifications like a quasistatic treatment neglecting displacement currents are being used to facilitate a direct current quantification without extensive numerical simulations. The measured B_1^+ magnitude at a certain radius from the conductor can be converted into the magnitude of the current by applying a simplified Ampere's circuit law.[88,90,91] The background signal around the lead, which in vivo is often inhomogeneous, represents a source of error for magnitude-based methods. A way to suppress this background signal is by using reversed RF polarization on the transmitter and receiver[88] (Fig. 9). This way, ideally only the implant coupling is visualized in the MR image and can be used to determine the current amplitude. On the receiver side, reverse polarization reconstruction is intrinsic to the acquired dataset, while on the transmit side parallel-transmit (pTx) systems with ≥2 channels would allow for reversed polarization during transmission.

Another method to quantify induced currents is based on analyzing the phase of an MR image around the implant.[92] This way, RF-induced implant currents can be detected with a low-SAR prescan sequence that poses no hazard in itself. Since the rms averaged RF current in the implant is proportional to $B_{1,\mathrm{RMS}}^+$, the result from the prescan can easily be scaled to subsequent imaging sequences at higher SAR levels. Compared to magnitude-based methods, phase-based current measurements are potentially faster, independent of proton-density weighting, and have lower SNR requirements. A disadvantage of phase-based methods is their sensitivity to gradient nonlinearities and phase variations of other origin, such as frequency shifts due to temperature variations, susceptibility jumps at interfaces, or blood flow. To reduce these influences, short echo times combined with a fast readout using an ultrashort echo time (UTE) sequence were applied in vivo and demonstrated the ability to characterize RF currents within an accuracy of ~10 mA/μT.[93] Based on these measurements and some simplifying assumptions, the corresponding RF heating could be predicted accurately. Another relatively simple method to assess not only the current magnitude but also its phase in vivo is based on using multichannel receive coils; it was applied for analyzing the image artifact around a deep-brain stimulation (DBS) lead.[94] Typically, two null-locations can be identified in the signal intensity emerging from the transmitter and receiver separately. Since the location of the receiver-null is independent of the transmitter and different for each receiver element, the receiver-null and transmitter-null locations can be identified independently, by inspecting the images from each receive-coil element separately. The phase of the current can then be calculated from the geometric null location and is an important parameter to allow mitigation of RF-induced currents on the DBS lead using pTx systems.[94]

The MR-based determination of the TF[47,95] represents another promising approach to measure implant currents. This expands the TF approach beyond phantoms to more complex exposure scenarios with realistic tissue heterogeneity, implant geometry, and location. The methodology uses the wire-like implant as a transceiver antenna. The implant is excited via a coaxial cable soldered to its tip and the resulting current distribution along its trajectory—reflecting the TF, by virtue of the principle of reciprocity—can be measured by MRI.[47,50] The necessity to connect a cable to the implant

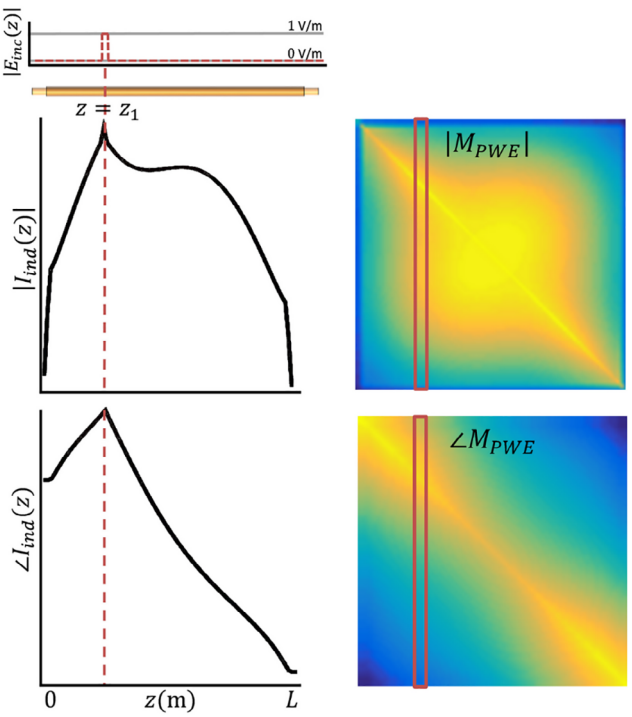

FIGURE 10: Simulation-based construction of the transfer matrix by applying a localized incident electric field. The rows of the transfer matrix are the current distributions for the various excitations. The transfer function is the first column of the transfer matrix. The transfer matrix for an implant can be determined solely by MR measurements ($|B_1^+|$ and transceiver phase distributions) (figure from Tokaya et al, 2019, Ref. 96).

modifies the TF, however, and prevents in vivo applications. This restriction was overcome by the introduction of the transfer matrix. This approach measures the RF-induced currents in the implant directly and without the need of any galvanic contact from MR measurements alone[95,96] (Fig. 10). The transfer matrix derived from these data contains not only the full TF, but additionally determines the total current along the implant for a given exposure situation. This allows not only to fully evaluate *tip* heating based on an incident background field, but also to assess other locations of potential RF heating along the implant. Like its "ancestor" TF, the transfer matrix describes how the implant responds to a preexisting background *E*-field. The latter must be known, therefore; that is, simulations are still required while the aforementioned sensor-based methods are, in principle, independent of such prior knowledge. The techniques applied for transfer-matrix acquisition have similarities with electric-properties tomography (EPT),[97,98] and consequently share some of its problems as well, most notably the transceiver-phase approximation and assumptions on the vector orientation of B_1^+ and *E*.

Most of these described MR-based techniques to assess implant safety still need further investigation, in particular if more complex implant geometries or locations, multiple implants, or complex lead trajectories come into play. Also, most of these MR-based current-measurement techniques assume a homogeneous or known B_1 transmit and/or receive field to work accurately.[93,94] These assumptions are increasingly difficult to fulfil at higher field strengths, which may limit the general applicability of such methods.

Current measurements are only an indirect measure of implant heating: they rely on thermal models that might be incomplete (eg, neglecting perfusion or thermoregulation). Measuring temperatures around the implant is a more direct assessment of implant safety and a variety of temperature-dependent MR contrasts exist that can be exploited for that purpose.[99,100] As of today, however, MR thermometry could not replace RF-power monitoring in conjunction with dedicated SAR models as an MR safety monitor. One reason is its vulnerability to subject-specific error sources, which may compromise temperature-reading accuracy in vivo beyond acceptable levels. In the presence of implants, accurate MR thermometry is even more challenging due to additional artifacts and signal voids around implants. Nevertheless, several studies have been performed showing the potential of MR thermometry around implants to assess implant heating with reasonable accuracies compared to fiberoptic temperature probes.[44,101,133–135] More weight is needed behind the development and validation of robust, fast, and accurate MR thermometry for in vivo applications around implants, which has a huge potential impact on patient safety.

Mitigation Strategies

Mitigation strategies, that is, active countermeasures against implant heating, can target either the background *E*-field the

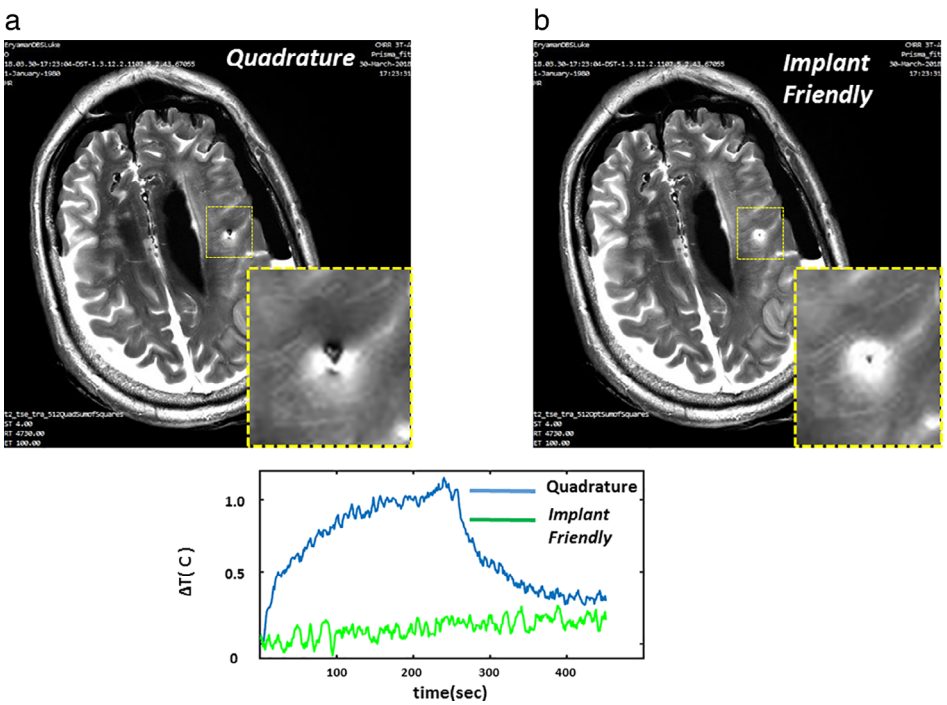

FIGURE 11: Detection and mitigation of RF-induced tip heating of a DBS implant in a cadaver brain using an MR image-based method and a 2-channel parallel-transmission system. For the "implant friendly" mode RF-induced tip heating was reduced substantially vs. the quadrature mode, while at the same time image quality is improved (figure from Eryaman et al, 2019, Ref. 94).

implant is exposed to or the scattered *E*-field generated by the implant. The latter call for the implant manufacturer to modify the implant in terms of geometry, size, or materials, while the former addresses the scanner manufacturer as it requires variations in RF-coil design or transmission-field properties to reduce heating independently of the implant type. Mitigation of gradient heating is not yet supported by device or scanner manufacturers. So far, it is up to the operator's common sense to avoid critical scenarios.

Implant Geometry and Materials

Suppressing RF-induced currents by eliminating all electrically conductive material from the implant is the ideal solution but rarely feasible. Other alterations of the implant structure can be implemented, which at least reduce RF-induced currents and possibly allow shifting their occurrence to less critical areas. These techniques can be grouped into the following approaches:

(a) Increasing the resistivity of the implant reduces the induced currents.[102–104]
(b) Increasing the capacitance (permittivity and thickness) and conductivity of the insulation around the conductor attenuates the wave propagation along the conductor.[105]
(c) Implementing RF chokes or traps, that is, resonating circuits tuned to block RF currents at the Larmor frequency.[104,106,107]
(d) Adding inductances (eg, by helical winding of 1D implants) or capacitances (eg, by adding dielectric materials) along the conductive lengths of the implant.[108–111] This way, low-pass or high-pass filters are implemented, blocking or reducing RF-induced currents along the implant.
(e) Cloaking the implant by, for example, metamaterials to reduce RF interactions.[112,113]

While approaches a), b), and e) focus on reducing the magnitude of the induced current, approaches c) and d) change the effective resonant length of the wire/implant. In the latter case, the result is frequency-dependent, implying that the same configuration that is safely reducing heating at 1.5T might not be working effectively at 3T, and vice versa.

Parallel Transmission

Each RF coil produces a characteristic *E*-field distribution inside the human body. If a second coil element with another characteristic *E*-field distribution is added, the overall incident *E*-field is a coherent superposition of both *E*-field vectors. In particular, the phase difference, which allows the incident *E*-field vectors to be of opposite direction at a particular location, provides an opportunity to reduce the background *E*-field in dedicated regions. Most important, the relative pulse amplitudes and phases for different coil elements can be changed at the sequence level, without hardware modifications, and—at least in principle—in real time. A birdcage RF coil, the standard body-coil design for many clinical MR systems, consists of two ports driven with a 90° phase difference to achieve the CP or "quadrature" mode. If the two channels, however, are driven individually as two independent linear polarization modes, the *E*-field distribution in the body can change completely. It has been demonstrated that the linear mode has *E*-field null zones in which an implant would be exposed to highly reduced background *E*-fields, hence strongly reduced RF heating.[114] If the linear birdcage modes are combined accordingly to reduce the RF current on an implant or lead, this 2-channel pTx system effectively mitigates RF heating[94,115,116] (Fig. 11).

Increasing the number of pTx channels increases the degrees of freedom to reduce the *E*-field near the implant, and hence suppress unwanted hotspots, with minimal loss of diagnostic image quality[117–121] (Fig. 12). This is achieved in an optimization process that also reveals the worst-case and best-case RF heating scenarios for a particular implant and

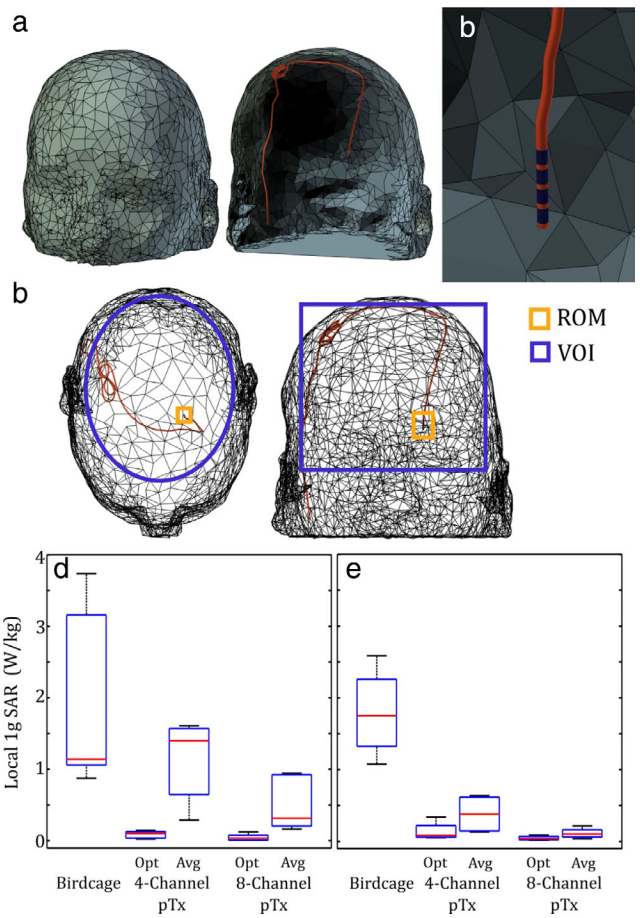

FIGURE 12: Simulation-based parallel-transmit (pTx) mitigation of RF-induced tip heating of deep-brain-stimulator leads based on realistic trajectories and models obtained from patient data. A higher number of pTx channels reduces the absolute induced implant SAR values and decreases their standard deviation across the simulated patient population (figure from Mc Elcheran et al, 2019, Ref. 122).

RF coil configuration, indicating the potential safety risk margins.[123,124] It has been demonstrated that an 8-channel pTx coil outperforms a 4-channel pTx coil in suppressing unwanted SAR hotspots induced by DBS leads.[121,122,125] Other constraints that can be embedded in the RF-pulse optimization process are local SAR, whole-body SAR, adaptive SAR,[126] or the *k*-space trajectory for spokes pulses.[118]

These pTx techniques are not restricted to proof-of-concept studies in phantoms on simplified implant geometries under controlled conditions; they could be an actual game changer for patients with complex implant geometries. This was recently demonstrated by two independent simulation studies investigating pTx mitigation of RF-induced heating of DBS leads with realistic trajectories extracted from CT-based patient data[121,122] (Fig. 12). Those works show that local SAR can be decreased by more than 94% compared to body-coil excitation at comparable B_1^+ homogeneity and global SAR. pTx based mitigation of implant heating is not restricted to simulation-based approaches, however. It has been shown that current sensors[120,124] or time-domain E-field probes[127] provide sufficient information to reduce tip heating substantially, using a pTx system. These results suggest that pTx systems could be a viable strategy to deal with the increasing complexity and number of medical implants in

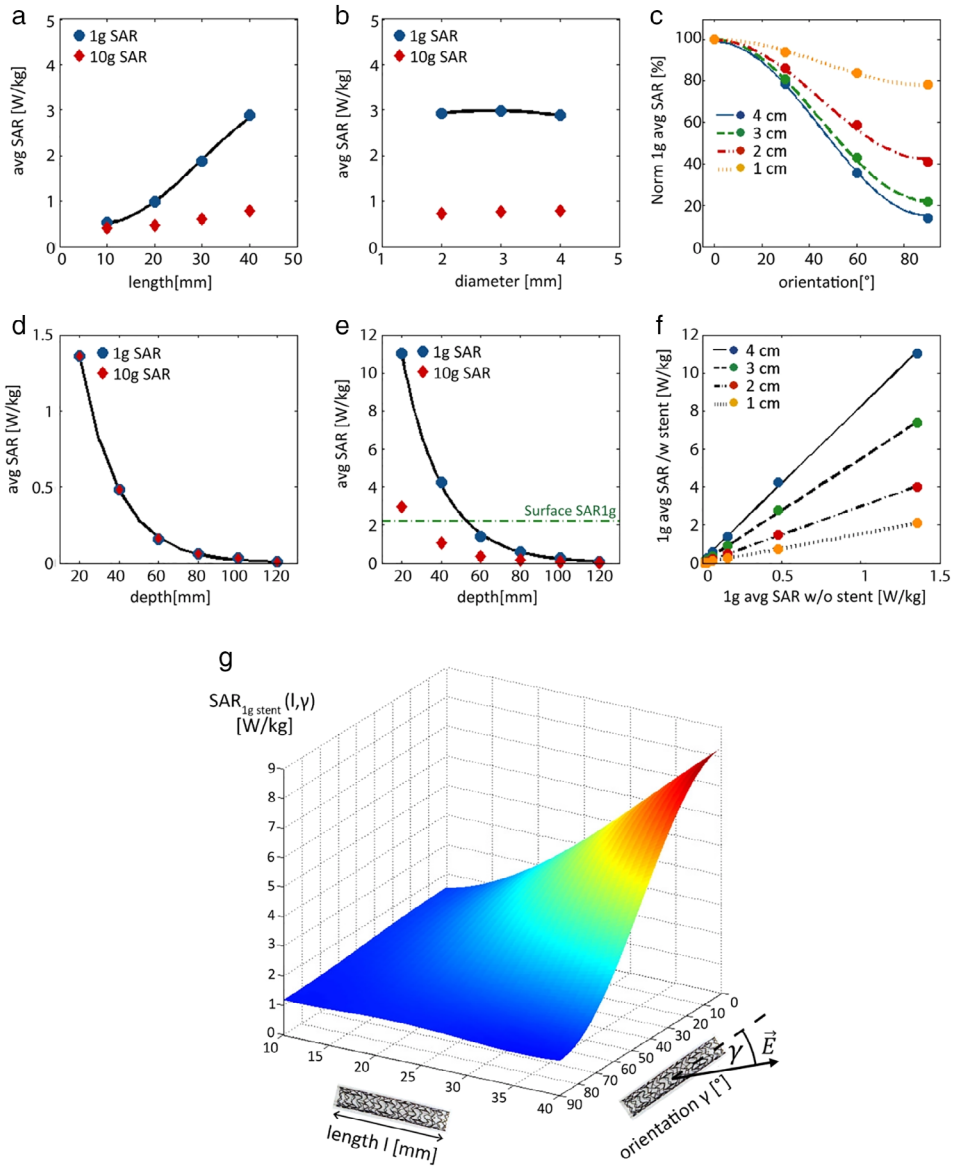

FIGURE 13: Simulated results for the RF-induced heating of a coronary stent as a function of different parameters (stent length, stent diameter, stent orientation, background local SAR). The data can be fitted to empirical functions in an *n*-dimensional parameter space, which can then be used to estimate the maximum induced stent SAR values for a given background local SAR in a human body model. This simulation-based parametrization approach for short implants gives a fast estimation of RF-induced heating and would enable a more generalized risk assessment of implant types instead of performing a full safety assessment for each new implant design (figure from Winter et al, 2015, Ref. 44).

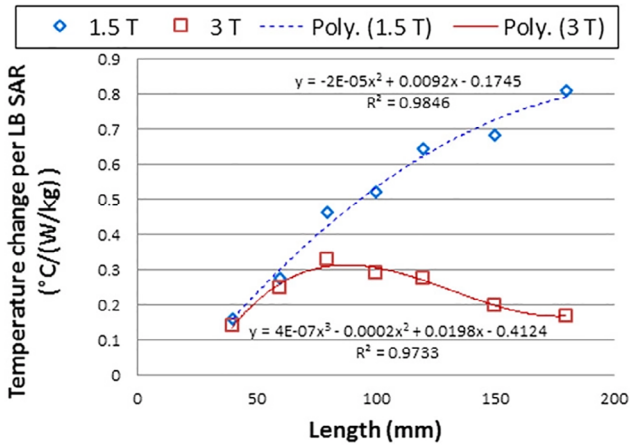

FIGURE 14: Temperature increase per local background SAR for different stent lengths. RF heating experiments in phantoms according to ASTM F2182 (figure from Song et al, 2018, Ref. 132).

MRI patients. However, more validation studies are needed to support this claim. Access to robust and flexible pTx system hardware is still very limited. Efforts exist, however, to attend to this need such as the development of an open-source hardware-based pTx implant-safety testbed, which is adaptable to experiments with up to 32 channels at all relevant field strengths (B_0 = 1.5 − 7 T).[127]

Other Techniques

If pTx hardware is not available, other methods can be applied to reduce implant heating by shaping the RF field. The linear-polarization mode of the birdcage RF coil has regions of reduced *E*-field and if these regions overlap with the implant, RF-induced currents are reduced.[114] If a birdcage coil had multiple ports along its circumference, one could "rotate" the linear-polarization mode by changing the feeding port. Similarly, a birdcage coil in linear-polarization mode with a single transmit channel can be physically rotated to align the low E-field zone with the implant.[128] This concept has been applied to DBS electrodes and showed significant improvement compared to the standard CP mode of the same birdcage coil.[129] Another mitigation approach that does not relying on pTx technology or modified RF-coil hardware is to put high-permittivity material pads on the subject at strategic locations. The high-permittivity dielectric modifies the background-field and it has been demonstrated that this can be efficiently used to reduce RF-induced tip heating.[130]

Conclusion

This article reviewed the existing literature on implant-related heating in MRI. A number of topics had to be excluded because of space limitations; for example, interventional devices or low-power sequences.

Implant safety is a thriving field in MRI; much has been accomplished but even more is still missing. Three international standards are the most relevant in this field: the MRI standard IEC 60601–2-33 and the implant standards ASTM F2182 and ISO/TS 10974. The latter set their scopes either on "passive" (ASTM) or "active" (ISO) implants. From the implant manufacturer's point of view, this distinction is fundamental, since active implants need EMC testing, while passive implants do not. From an MRI perspective, however, this distinction appears less relevant. Passive-implant hazards are a subset of active-implant hazards; they are comprehensively covered by the ISO/TS 10974 too. The ASTM F2182 was a significant milestone and many of its procedural developments will live on. But no reasons exist, in these authors' opinion, to maintain two implant standards in parallel. ISO/TS 10974 is in many respects more modern and more general; all implants, active or passive, should be tested against it. Low-cost procedures for low-risk implants would be on the wish list for future editions; for example, recipes to easily translate an existing safety-assessment from, say, one fixation plate to a similar one. The concept of an empirical parametrization of the implant-related hazard as demonstrated in Ref. 44 may be helpful in this context (Fig. 13).

The scarce available literature on gradient heating suggests that excessive heating occurs only in unfavorable cases. Nevertheless, such cases are possible, and it is unsatisfactory that presently neither the scanner nor the implant manufacturer inform the operator when a critical situation arises and how to avoid it.

Accurate numerical simulations are the key to implant safety: they have reached a high level of maturity and they provide both insight and practical solutions. Future developments must aim to treat complex implants in realistic detail. So far, ISO/TS 10974's Tier 4 is only conceptual but has not yet any practical value. Simulations need validation, however, and measurements are often restricted to phantoms. This is acceptable as long as phantom measurements are not misunderstood as predictive for the in vivo case. Phantom experiments are a testbed to validate the simulation methodology, coil models, etc., which are then identically applied to anatomical voxel models.

Ex-ante simulations of some numerical model remain surrogates, however. Ultimately, any safety assessment must be specific to the given subject, implant, and scan conditions. This means that implant and scanner must communicate, in some way; the implant must inform the scanner about its presence and condition and the scanner must be able to respond to this input. The combination of real-time sensors (eg, temperature, current, *E*-field, etc.) on the implant and a pTx system on the scanner would be most helpful to achieve this goal but other approaches are certainly conceivable.

In implant-safety discussions it is often taken for granted that lower field strengths automatically reduce the risk. ISO/TS 10974 or the Fixed-Parameter Option were initially conceived for 1.5T but not for 3T, and recently the idea

of dedicated low-field scanners with $B_0 \approx 0.5T$ is gaining new attention.[131] Conceptually, the translation of $B^+_{1,\mathrm{RMS}}$ into implant SAR, for example, at the tip of a pacemaker lead, is a two-step process, however. First, $B^+_{1,\mathrm{RMS}}$ creates a background *E*-field. This effect scales with the *frequency*, hence B_0, and the lower field has the safety edge. In the second step, background *E*-field creates a tip *E*-field and this conversion scales linearly with the RF *wavelength* in tissue (as long as half this wavelength is shorter than the implant and the body coil). This time the *higher* field wins. Qualitatively, this effect can be seen in Fig. 14.[132] There is no universal answer to the question of a safest field strength; therefore, the individual implant, RF coil, and scan conditions must be considered.

Acknowledgments

The authors thank Alessandro Arduino, Oriano Bottauscio, Rüdiger Brühl, Mario Chiampi, Niels Kuster, Johannes Petzold, Berk Silemek, and Umberto Zanovello for many helpful discussions.

References

1. Davis P, Crooks L, Arakawa M, McRee R, Kaufman L, Margulis A. Potential hazards in NMR imaging: Heating effects of changing magnetic fields and RF fields on small metallic implants. Am J Roentgenol 1981;137:857-860.
2. Nyenhuis JA, Park S-M, Kamondetdacha R, Amjad A, Shellock FG, Rezai AR. MRI and implanted medical devices: Basic interactions with an emphasis on heating. IEEE Trans Device Mater Reliab 2005;5: 467-480.
3. Baker KB, Tkach JA, Nyenhuis JA, et al. Evaluation of specific absorption rate as a dosimeter of MRI-related implant heating. J Magn Reson Imaging 2004;20:315-320.
4. Irnich W, Irnich B, Bartsch C, Stertmann WA, Gufler H, Weiler G. Do we need pacemakers resistant to magnetic resonance imaging? Europace 2005;7:353-365.
5. Ferris NJ, Kavnoudias H, Thiel C, Stuckey S. The 2005 Australian MRI safety survey. Am J Roentgenol 2007;188:1388-1394.
6. Kanal E, Barkovich AJ, Bell C, et al. ACR guidance document on MR safe practices: 2013. J Magn Reson Imaging 2013;37:501-530.
7. Nutt J, Anderson V, Peacock JH, Hammerstad J, Burchiel K. DBS and diathermy interaction induces severe CNS damage. Neurology 2001; 56:1384-1386.
8. Spiegel J, Fuss G, Backens M, et al. Transient dystonia following magnetic resonance imaging in a patient with deep brain stimulation electrodes for the treatment of Parkinson disease: Case report. J Neurosurg 2003;99:772-774.
9. Henderson JM, Tkach J, Phillips M, Baker K, Shellock FG, Rezai AR. Permanent neurological deficit related to magnetic resonance imaging in a patient with implanted deep brain stimulation electrodes for Parkinson's disease: Case report. Neurosurgery 2005;57:E1063.
10. Rezai AR, Finelli D, Nyenhuis JA, et al. Neurostimulation systems for deep brain stimulation: in vitro evaluation of magnetic resonance imaging–related heating at 1.5 Tesla. J Magn Reson Imaging 2002; 15:241-250.
11. Rezai AR, Phillips M, Baker KB, et al. Neurostimulation system used for deep brain stimulation (DBS): MR safety issues and implications of failing to follow safety recommendations. Invest Radiol 2004;39: 300-303.
12. Zanchi MG, Venook R, Pauly JM, Scott GC. An optically coupled system for quantitative monitoring of MRI-induced RF currents into long conductors. IEEE Trans Med Imaging 2010;29:169-178.
13. Kraff O, Quick HH. Sicherheit von Implantaten im Hochfeld-und Ultrahochfeld-MRT. Radiologe 2019;59:898-905.
14. ISMRM & SMRT MR Safety Resources. Available from https://www.ismrm.org/mr-safety-links/
15. MRI Safety Home. Available from http://www.mrisafety.com/
16. Dempsey MF, Condon B, Hadley DM. Investigation of the factors responsible for burns during MRI. J Magn Reson Imaging 2001;13: 627-631.
17. Brühl R, Ihlenfeld A, Ittermann B. Gradient heating of bulk metallic implants can be a safety concern in MRI. Magn Reson Med 2017;77: 1739-1740.
18. Zilberti L, Arduino A, Bottauscio O, Chiampi M. The underestimated role of gradient coils in MRI safety. Magn Reson Med 2017;77:13-15.
19. Graf H, Steidle G, Schick F. Heating of metallic implants and instruments induced by gradient switching in a 1.5-Tesla whole-body unit. J Magn Reson Imaging 2007;26:1328-1333.
20. Bannan KE, Handler W, Chronik B, Salisbury SP. Heating of metallic rods induced by time-varying gradient fields in MRI. J Magn Reson Imaging 2013;38:411-416.
21. Zilberti L, Bottauscio O, Chiampi M, Hand J, Lopez HS, Crozier S. Collateral thermal effect of MRI-LINAC gradient coils on metallic hip prostheses. IEEE Trans Magn 2014;50:1-4.
22. Zilberti L, Bottauscio O, Chiampi M, et al. Numerical prediction of temperature elevation induced around metallic hip prostheses by traditional, split, and uniplanar gradient coils. Magn Reson Med 2015; 74:272-279.
23. Arduino A, Bottauscio O, Brühl R, Chiampi M, Zilberti L. In silico evaluation of the thermal stress induced by MRI switched gradient fields in patients with metallic hip implant. Phys Med Biol 2019;64:245006.
24. Pennes HH. Analysis of tissue and arterial blood temperatures in the resting human forearm. Appl Physiol 1948;1:93-122.
25. Wissler EH. Pennes' 1948 paper revisited. J Appl Physiol 1998;85: 35-41.
26. EM and thermal tissue parameter database. Available from https://itis.swiss/virtual-population/tissue-properties/database/database-summary/
27. Collins CM, Liu W, Wang J, et al. Temperature and SAR calculations for a human head within volume and surface coils at 64 and 300 MHz. J Magn Reson Imaging 2004;19:650-656.
28. van Rhoon GC, Samaras T, Yarmolenko PS, Dewhirst MW, Neufeld E, Kuster N. CEM43°C thermal dose thresholds: A potential guide for magnetic resonance radiofrequency exposure levels? Eur Radiol 2013; 23:2215-2227.
29. Sapareto SA, Dewey WC. Thermal dose determination in cancer therapy. Int J Radiat Oncol Biol Phys 1984;10:787-800.
30. Yarmolenko PS, Moon EJ, Landon C, et al. Thresholds for thermal damage to normal tissues: An update. Int J Hyperthermia 2011;27: 320-343.
31. Murbach M, Neufeld E, Capstick M, et al. Thermal tissue damage model analyzed for different whole-body SAR and scan durations for standard MR body coils: Thermal dose and tissue damage in MR RF heating. Magn Reson Med 2014;71:421-431.
32. Nordbeck P, Fidler F, Weiss I, et al. Spatial distribution of RF-induced E-fields and implant heating in MRI. Magn Reson Med 2008;60: 312-319.
33. Woods TO. Standards for medical devices in MRI: Present and future. J Magn Reson Imaging 2007;26:1186-1189.
34. Food and Drug Administration (FDA): Establishing safety and compatibility of passive implants in the magnetic resonance (MR) environment — Guidance for industry and Food and Drug Administration Staff. 2014.

35. Food and Drug Administration (FDA): Assessment of radiofrequency-induced heating in the magnetic resonance (MR) environment for multi-configuration passive medical devices — Guidance for industry and Food and Drug Administration Staff. 2016.

36. International Electrotechnical Commission (IEC): IEC 60601–2-33:2010 +AMD1:2013+AMD2:2015 CSV: Medical electrical equipment — particular requirements for the basic safety and essential performance of magnetic resonance equipment for medical diagnosis, Edition 3.2. 2015.

37. F2182-11a: Standard test method for measurement of radio frequency induced heating on or near passive implants during magnetic resonance imaging. 2019.

38. International Organization for Standardization (ISO): Assessment of the safety of magnetic resonance imaging for patients with an active implantable medical device. Tech Specif ISOTS 10974 2018; second edition.

39. ASTM F2503–13: Standard practice for marking medical devices and other items for safety in the magnetic resonance environment. 2013.

40. Food and Drug Administration (FDA): Testing and labeling medical devices for safety in the magnetic resonance (MR) environment. Draft guidance for industry and Food and Drug Administration Staff. 2019.

41. Park S-M, Kamondetdacha R, Nyenhuis JA. Calculation of MRI-induced heating of an implanted medical lead wire with an electric field transfer function. J Magn Reson Imaging 2007;26:1278-1285.

42. Umashankar K, Taflove A. A novel method to analyze electromagnetic scattering of complex objects. IEEE Trans Electromagn Compat 1982; EMC-24:397-405.

43. Li BK, Liu F, Weber E, Crozier S. Hybrid numerical techniques for the modeling of radiofrequency coils in MRI. NMR Biomed 2009;22: 937-951.

44. Winter L, Oberacker E, Özerdem C, et al. On the RF heating of coronary stents at 7.0 Tesla MRI. Magn Reson Med 2015;74:999-1010.

45. Santoro D, Winter L, Müller A, et al. Detailing radio frequency heating induced by coronary stents: A 7.0 Tesla magnetic resonance study. PLoS One 2012;7:e49963.

46. Yeung CJ, Susil RC, Atalar E. RF safety of wires in interventional MRI: Using a safety index. Magn Reson Med 2002;47:187-193.

47. Tokaya JP, Raaijmakers AJE, Luijten PR, Bakker JF, van Den Berg CA. MRI-based transfer function determination for the assessment of implant safety. Magn Reson Med 2017;78:2449-2459.

48. Attaran A, Handler WB, Wawrzvn K, Chronik BA: Development of a transfer-function measurement procedure for the evaluation's of MRI-conditional medical devices at 3T. In 2018 IEEE Can Conf Electr Comput Eng CCECE; 2018:1–4.

49. Missoffe A, Aissani S. Experimental setup for transfer function measurement to assess RF heating of medical leads in MRI: Validation in the case of a single wire. Magn Reson Med 2018;79:1766-1772.

50. Feng S, Qiang R, Kainz W, Chen J. A technique to evaluate MRI-induced electric fields at the ends of practical implanted lead. IEEE Trans Microw Theory Tech 2015;63:305-313.

51. Feng S, Wang Q, Wen C, Zheng J, Kainz W, Chen J. Simplified transfer function assessment of implantable leads for MRI safety evaluations. IEEE Trans Electromagn Compat 2019;61:1432-1437.

52. Fiedler TM, Ladd ME, Bitz AK. SAR simulations & safety. Neuroimage 2018;168:33-58.

53. Murbach MJ. EMF risk assessment: Exposure assessment and safety considerations in MRI and other environments (Doctoral Thesis). ETH Zürich 2013. https://doi.org/10.3929/ethz-a-010080329

54. Ittermann B, Bottauscio O, Hand J, et al.: Metrology for MRI Safety. In 17th Int Congr Metrol. EDP Sciences; 2015:09001.

55. Noureddine Y, Kraff O, Ladd ME, et al. In vitro and in silico assessment of RF-induced heating around intracranial aneurysm clips at 7 Tesla. Magn Reson Med 2018;79:568-581.

56. Noureddine Y, Kraff O, Ladd ME, et al. Radiofrequency induced heating around aneurysm clips using a generic birdcage head coil at 7 Tesla under consideration of the minimum distance to decouple multiple aneurysm clips. Magn Reson Med 2019;82:1859-1875.

57. Murbach M, Neufeld E, Cabot E, et al. Virtual population-based assessment of the impact of 3 Tesla radiofrequency shimming and thermoregulation on safety and B_1 + uniformity: Safety and thermoregulation in 3T RF shimming. Magn Reson Med 2016;76:986-997.

58. Adriany G, de Moortele P-FV, Wiesinger F, et al. Transmit and receive transmission line arrays for 7 Tesla parallel imaging. Magn Reson Med 2005;53:434-445.

59. Vaughan JT, Adriany G, Snyder CJ, et al. Efficient high-frequency body coil for high-field MRI. Magn Reson Med 2004;52:851-859.

60. Gosselin M-C, Neufeld E, Moser H, et al. Development of a new generation of high-resolution anatomical models for medical device evaluation: The virtual population 3.0. Phys Med Biol 2014;59:5287-5303.

61. Saito K, Sato K, Kinase S, Nagaoka T. Japanese Computational Phantoms: Otoko, Onago, JM, JM2, JF, TARO, HANAKO, Pregnant Woman, and Deformable Child. In: *Handbook of anatomical models for radiation dosimetry*. Xu XG, and Eckerman KF [eds.], Boca Raton, FL: CRC Press; 2010:221-253.

62. Ackerman MJ. The visible human project. Proc IEEE 1998;86:504-511.

63. Makarov SN, Noetscher GM, Yanamadala J, et al. Virtual human models for electromagnetic studies and their applications. IEEE Rev Biomed Eng 2017;10:95-121.

64. Gabriel S, Lau RW, Gabriel C. The dielectric properties of biological tissues: II. Measurements in the frequency range 10 Hz to 20 GHz. Phys Med Biol 1996;41:2251-2269.

65. Oberacker E, Paul K, Huelnhagen T, et al. Magnetic resonance safety and compatibility of tantalum markers used in proton beam therapy for intraocular tumors: A 7.0 Tesla study. Magn Reson Med 2017;78: 1533-1546.

66. Destruel A, O'Brien K, Jin J, Liu F, Barth M, Crozier S. Adaptive SAR mass-averaging framework to improve predictions of local RF heating near a hip implant for parallel transmit at 7 T. Magn Reson Med 2019; 81:615-627.

67. Murbach M, Neufeld E, Kainz W, Pruessmann KP, Kuster N. Whole-body and local RF absorption in human models as a function of anatomy and position within 1.5T MR body coil: MR RF exposure as a function of large-scale anatomical properties. Magn Reson Med 2014; 71:839-845.

68. Kotte A, van Leeuwen G, de Bree J, van der Koijk J, Crezee H, Lagendijk J. A description of discrete vessel segments in thermal modeling of tissues. Phys Med Biol 1996;41:865-884.

69. Kok HP, Gellermann J, van den Berg CAT, Stauffer PR, Hand JW, Crezee J. Thermal modeling using discrete vasculature for thermal therapy: A review. Int J Hyperthermia 2013;29:336-345.

70. Shrivastava D, Utecht L, Tian J, Hughes J, Vaughan JT. In vivo radiofrequency heating in swine in a 3T (123.2-MHz) birdcage whole body coil: in vivo RF heating in 3T. Magn Reson Med 2014;72:1141-1150.

71. Zienkiewicz OC, Taylor RL. *The finite element method for solid and structural mechanics*: Oxford, UK: Butterworth-Heinemann; 2005.

72. Szczerba D, Neufeld E, Zefferer M, Buhlmann B, Kuster N: FEM based morphing of whole body human models. In 2011 XXXth URSI gen Assem Sci Symp. Istanbul: IEEE; 2011:1–3.

73. Avants BB, Epstein CL, Grossman M, Gee JC. Symmetric diffeomorphic image registration with cross-correlation: Evaluating automated labeling of elderly and neurodegenerative brain. Med Image Anal 2008;12:26-41. [Special Issue on the Third International Workshop on Biomedical Image Registration — WBIR 2006].

74. Akbarzadeh A, Gutierrez D, Baskin A, et al. Evaluation of whole-body MR to CT deformable image registration. J Appl Clin Med Phys 2013; 14:238-253.

75. Tward D, Ceritoglu C, Sturgeon G, Segars WP, Miller M, Ratnanather J: Generating patient-specific dosimetry phantoms with whole-body

diffeomorphic image registration. In Bioeng Conf NEBEC 2011 IEEE 37th Annu Northeast. IEEE; 2011:1–2.

76. ISO/TR 21900: Guidance for uncertainty analysis regarding the application of ISO/TS 10974. 2018.

77. Weidemann G, Seifert F, Hoffmann W, Ittermann B. RF current measurements in implanted wires in phantoms by fiber optic current clamps. Proc Intl Soc Mag Reson Med 2015;23:1852.

78. Silemek B, Acikel V, Oto C, et al. A temperature sensor implant for active implantable medical devices for in vivo subacute heating tests under MRI. Magn Reson Med 2018;79:2824-2832.

79. Graesslin I, Krueger S, Vernickel P, Achtzehn J, Nehrke K, Weiss S. Detection of RF unsafe devices using a parallel transmission MR system. Magn Reson Med 2013;70:1440-1449.

80. Ellenor CW, Stang PP, Etezadi-Amoli M, Pauly JM, Scott GC. Offline impedance measurements for detection and mitigation of dangerous implant interactions: An RF safety prescreen. Magn Reson Med 2015; 73:1328-1339.

81. Graesslin I, Vernickel P, Börnert P, et al. Comprehensive RF safety concept for parallel transmission MR. Magn Reson Med 2015;74: 589-598.

82. Luechinger R, Zeijlemaker VA, Pedersen EM, et al. In vivo heating of pacemaker leads during magnetic resonance imaging. Eur Heart J 2005;26:376-383.

83. Winkler SA, Picot PA, Thornton MM, Rutt BK. Direct SAR mapping by thermoacoustic imaging: A feasibility study. Magn Reson Med 2017; 78:1599-1606.

84. Dixit N, Stang PP, Pauly JM, Scott GC. Thermo-acoustic ultrasound for detection of RF-induced device lead heating in MRI. IEEE Trans Med Imaging 2018;37:536-546.

85. Acikel V, Uslubas A, Atalar E. Modeling of electrodes and implantable pulse generator cases for the analysis of implant tip heating under MR imaging. Med Phys 2015;42:3922-3931.

86. Camacho CR, Plewes DB, Henkelman RM. Nonsusceptibility artifacts due to metallic objects in MR imaging. J Magn Reson Imaging 1995; 5:75-88.

87. Scott GC, Joy MLG, Armstrong RL, Henkelman RM. Electromagnetic considerations for RF current density imaging [MRI technique]. IEEE Trans Med Imaging 1995;14:515-524.

88. Overall WR, Pauly JM, Stang PP, Scott GC. Ensuring safety of implanted devices under MRI using reversed RF polarization. Magn Reson Med 2010;64:823-833.

89. Graf H, Steidle G, Martirosian P, Lauer UA, Schick F. Effects on MRI due to altered RF polarrfization near conductive implants or instruments. Med Phys 2006;33:124-127.

90. Venook RD, Overall WR, Shultz K, Conolly S, Pauly JM, Scott GC. Monitoring induced currents on long conductive structures during MRI. Proc Intl Soc Mag Reson Med 2008;16:898.

91. van den Bosch MR, Moerland MA, Lagendijk JJ, Bartels LW, van den Berg CA. New method to monitor RF safety in MRI-guided interventions based on RF induced image artefacts. Med Phys 2010;37: 814-821.

92. Griffin GH, Anderson KJT, Celik H, Wright GA. Safely assessing radiofrequency heating potential of conductive devices using image-based current measurements. Magn Reson Med 2015;73:427-441.

93. Griffin GH, Ramanan V, Barry J, Wright GA. Toward in vivo quantification of induced RF currents on long thin conductors. Magn Reson Med 2018;80:1922-1934.

94. Eryaman Y, Kobayashi N, Moen S, et al. A simple geometric analysis method for measuring and mitigating RF induced currents on deep brain stimulation leads by multichannel transmission/reception. Neuroimage 2019;184:658-668.

95. Tokaya JP, Raaijmakers AJ, Luijten PR, van den Berg CA. MRI-based, wireless determination of the transfer function of a linear implant: Introduction of the transfer matrix. Magn Reson Med 2018;80:2771-2784.

96. Tokaya JP, Raaijmakers AJE, Luijten PR, Sbrizzi A. Berg CAT van den: MRI-based transfer function determination through the transfer matrix by jointly fitting the incident and scattered B_1^+ field. Magn Reson Med 2020;83:1081-1095.

97. Katscher U. Berg CAT van den: Electric properties tomography: Biochemical, physical and technical background, evaluation and clinical applications. NMR Biomed 2017;30:e3729.

98. Katscher U, Voigt T, Findeklee C, Vernickel P, Nehrke K, DÖssel O. Determination of electric conductivity and local SAR via B1 mapping. IEEE Trans Med Imaging 2009;28:1365-1374.

99. Rieke V, Butts Pauly K. MR thermometry. J Magn Reson Imaging 2008;27:376-390.

100. Winter L, Oberacker E, Paul K, et al. Magnetic resonance thermometry: Methodology, pitfalls and practical solutions. Int J Hyperthermia 2016;32:63-75.

101. Ehses P, Fidler F, Nordbeck P, et al. MRI thermometry: Fast mapping of RF-induced heating along conductive wires. Magn Reson Med 2008;60:457-461.

102. Angelone LM, Ahveninen J, Belliveau JW, Bonmassar G. Analysis of the role of lead resistivity in specific absorption rate for deep brain stimulator leads at 3T MRI. IEEE Trans Med Imaging 2010;29:1029-1038.

103. Mattei E, Calcagnini G, Censi F, Triventi M, Bartolini P. Role of the lead structure in MRI-induced heating: in vitro measurements on 30 commercial pacemaker/defibrillator leads. Magn Reson Med 2012;67: 925-935.

104. Bottomley PA, Kumar A, Edelstein WA, Allen JM, Karmarkar PV. Designing passive MRI-safe implantable conducting leads with electrodes. Med Phys 2010;37:3828-3843.

105. Golestanirad L, Angelone LM, Kirsch J, et al. Reducing RF-induced heating near implanted leads through high-dielectric capacitive bleeding of current (CBLOC). IEEE Trans Microw Theory Tech 2019; 67:1265-1273.

106. Griffin GH, Anderson KJT, Wright GA. Miniaturizing floating traps to increase RF safety of magnetic-resonance-guided percutaneous procedures. IEEE Trans Biomed Eng 2017;64:329-340.

107. Ladd ME, Quick HH. Reduction of resonant RF heating in intravascular catheters using coaxial chokes. Magn Reson Med 2000;43:615-619.

108. Ferhanoglu O, Eryaman Y, Atalar E. MRI compatible pacemaker leads. Proc Intl Soc Mag Reson Med 2005;13:963.

109. Baker KB, Tkach J, Hall JD, Nyenhuis JA, Shellock FG, Rezai AR. Reduction of magnetic resonance imaging-related heating in deep brain stimulation leads using a Lead management device. Oper Neurosurg 2005;57(suppl_4):ONS-392-ONS-397.

110. Liu Y, Kainz W, Qian S, Wu W, Chen J. Effect of insulating layer material on RF-induced heating for external fixation system in 1.5T MRI system. Electromagn Biol Med 2014;33:223-227.

111. Nordbeck P, Weiss I, Ehses P, et al. Measuring RF-induced currents inside implants: Impact of device configuration on MRI safety of cardiac pacemaker leads. Magn Reson Med 2009;61:570-578.

112. Zanovello U, Matekovits L, Zilberti L. An ideal dielectric coat to avoid prosthesis RF-artefacts in magnetic resonance imaging. Sci Rep 2017; 7:326.

113. Zanovello U, Zilberti L, Matekovits L. A near-field cloaking study to reduce MRI RF-artefacts in presence of elongated prostheses. IEEE J Electromagn RF Microw Med Biol 2018;2:249-256.

114. Eryaman Y, Akin B, Atalar E. Reduction of implant RF heating through modification of transmit coil electric field. Magn Reson Med 2011;65: 1305-1313.

115. Etezadi-Amoli M, Zanchi MG, Stang P, et al. Transmit array concepts for improved MRI safety in the presence of long conductors. Proc Intl Soc Mag Reson Med 2009;17:4801.

116. Eryaman Y, Turk EA, Oto C, Algin O, Atalar E. Reduction of the radiofrequency heating of metallic devices using a dual-drive birdcage coil. Magn Reson Med 2013;69:845-852.

117. Gudino N, Sonmez M, Yao Z, et al. Parallel transmit excitation at 1.5T based on the minimization of a driving function for device heating. Med Phys 2015;42:359-371.

118. Eryaman Y, Guerin B, Akgun C, et al. Parallel transmit pulse design for patients with deep brain stimulation implants. Magn Reson Med 2015;73:1896-1903.

119. Córcoles J, Zastrow E, Kuster N. Convex optimization of MRI exposure for mitigation of RF-heating from active medical implants. Phys Med Biol 2015;60:7293-7308.

120. Etezadi-Amoli M, Stang P, Kerr A, Pauly J, Scott G. Controlling radiofrequency-induced currents in guidewires using parallel transmit. Magn Reson Med 2015;74:1790-1802.

121. Guerin B, Angelone LM, Dougherty D, Wald LL. Parallel transmission to reduce absorbed power around deep brain stimulation devices in MRI: Impact of number and arrangement of transmit channels. Magn Reson Med 2020;83:299-311.

122. McElcheran CE, Golestanirad L, Iacono MI, et al. Numerical simulations of realistic lead trajectories and an experimental verification support the efficacy of parallel radiofrequency transmission to reduce heating of deep brain stimulation implants during MRI. Sci Rep 2019; 9:2124.

123. Seifert F, Weidemann G, Ittermann B. Q matrix approach to control implant heating by transmit array coils. Proc Intl Soc Mag Reson Med 2015;23:3212.

124. Godinez F, Scott G, Padormo F, Hajnal JV, Malik SJ. Safe guidewire visualization using the modes of a PTx transmit array MR system. Magn Reson Med 2020;83:2343-2355.

125. McElcheran CE, Yang B, Anderson KJ, Golestanirad L, Graham SJ. Parallel radiofrequency transmission at 3 Tesla to improve safety in bilateral implanted wires in a heterogeneous model. Magn Reson Med 2017;78:2406-2415.

126. Destruel A, Fuentes M, Weber E, et al. A numerical and experimental study of RF shimming in the presence of hip prostheses using adaptive SAR at 3T. Magn Reson Med 2019;81:3826-3839.

127. Winter L, Silemek B, Petzold J, Pfeiffer H, Hoffmann W, Seifert F, Ittermann B. Parallel transmission (pTx) medical implant safety testbed: real-time mitigation of RF induced tip heating using time-domain E-field sensors. Magn Reson Med 2020.

128. Golestanirad L, Keil B, Angelone LM, Bonmassar G, Mareyam A, Wald LL. Feasibility of using linearly polarized rotating birdcage transmitters and close-fitting receive arrays in MRI to reduce SAR in the vicinity of deep brain simulation implants. Magn Reson Med 2017;77: 1701-1712.

129. Golestanirad L, Iacono MI, Keil B, et al. Construction and modeling of a reconfigurable MRI coil for lowering SAR in patients with deep brain stimulation implants. Neuroimage 2017;147:577-588.

130. Yu Z, Xin X, Collins CM. Potential for high-permittivity materials to reduce local SAR at a pacemaker lead tip during MRI of the head with a body transmit coil at 3 T. Magn Reson Med 2017;78:383-386.

131. Campbell-Washburn AE, Ramasawmy R, Restivo MC, et al. Opportunities in interventional and diagnostic imaging by using high-performance low-field-strength MRI. Radiology 2019;293:384-393.

132. Song T, Xu Z, Iacono MI, Angelone LM, Rajan S. Retrospective analysis of RF heating measurements of passive medical implants. Magn Reson Med 2018;80:2726-2730.

133. Detti V, Grenier D, Perrin E, Beuf O. Assessment of radio frequency self-heating arounda metallic wire with MR T1-based thermometry. Magn Reson Med 2011;66:448-455

134. Gensler D, Fidler F, Ehses P, et al. MR safety: fast T_1 thermometry of the RF-induced heating of medical devices. Magn Reson Med 2012; 68:1593-9159.

135. Weber H, Taviani V, Yoon D, Ghanouni P, Pauly KB, Hargreaves BA. MR thermometry near metallic devices using multispectral imaging. Magn Reson Med 2017;77:1162-1169.